Nuclear Quadrupolar Resonance Structural Characterization of Halide Perovskites and Perovskitoids: A Roadmap from Electronic Structure Calculations for Lead–Iodide-Based Compounds

Claudio Quarti, Régis Gautier, Marios Zacharias, Axel Gansmuller, Claudine Katan

https://doi.org/10.1021/jacs.4c09877

NQR structural characterization of halide perovskites and perovskitoids: a roadmap from electronic structure calculations for lead-iodide based compounds

Claudio Quarti,[a]* Régis Gautier,[b] Marios Zacharias,[c] Axel Gansmuller,[d] Claudine Katan [b]*

[a] Laboratory for Chemistry of Novel Materials, Materials Research Institute, University of Mons-UMONS, Place du Parc 20, Mons B-7000, Belgium

[b] Univ Rennes, CNRS, Ecole Nationale Supérieure de Chimie de Rennes, ISCR - UMR6226, Rennes, France

[c] Univ Rennes, CNRS, INSA Rennes, Institut FOTON - UMR6082, Rennes, France

[d] Université de Lorraine, CNRS, CRM2 UMR 7036, F-54000 Nancy, France

* corresponding authors: Claudio.QUARTI@umons.ac.be, claudine.katan@univ-rennes.fr

Abstract

Metal halide perovskites, including some of their related perovskitoid structures, form a semiconductor class of their own, which is arousing ever-growing interest from the scientific community. With halides being involved in the various structural arrangements, namely pure corner sharing MX_6 (M is metal, X is halide) octahedra, for perovskite networks, or alternatively a combination of corner-, edge- and/or face-sharing for related perovskitoids, they represent the ideal probe for characterizing the way octahedra are linked together. Well-known for their inherently large quadrupolar constants, which is detrimental to the resolution of nuclear magnetic resonance (NMR) spectroscopy, most abundant halide isotopes ($^{35/37}$Cl, $^{79/81}$Br, ^{127}I) are in turn attractive for magnetic field-free, nuclear quadrupolar resonance (NQR) spectroscopy. Here we investigate the possibility of exploiting NQR spectroscopy of halides to distinctively characterize the various metal halide structural arrangements based on density functional theory (DFT). Our calculations nicely match the available experimental results. Furthermore, they demonstrate that compounds with different connectivity of their MX_6 building blocks, including lower dimensionalities such as 2D networks, show distinct NQR signals in a broad spectral window. They finally provide a roadmap of the characteristic NQR frequency ranges for each octahedral connectivity, which may be a useful guide to experimentalists, considering the long acquisition times typical of NQR. We hope this work will encourage the incorporation of NQR spectroscopy to complete our knowledge of the structural diversity of metal halides.

https://doi.org/10.1021/jacs.4c09877

Introduction

Halide Perovskites (HP) and perovskitoid compounds are currently at the center of a feverish research activity, following their record-breaking performances in photovoltaics.[1,2] Bulk 3-dimensional (3D),[1,2] 2-dimensional (2D),[3–9] and mixed HP 3D/2D phases,[10,11] are nowadays widely investigated as photoactive materials in solar cells and light-emitting devices, thanks to their large absorption coefficient (10^5 cm^{-1}),[12] suitable optical absorption energy onset,[12–14] and long carrier lifetimes and diffusion lengths.[15–17] Besides, these solution-processed compounds offer an unparalleled compositional and structural *tailorability*, paving the way for new functionalities, and fields of applications.[18–21] They indeed sustain different chemical compositions, as in the case of halide substitution (I→Br→Cl) and mixing.[13,22] In addition, they allow for the formation of very diverse atomistic nano-architectures. Considering the MX_6 (M=metal, X=halide) octahedra as fundamental building blocks, these may be organized in corner-shared, edge-shared and face-shared fashion, as illustrated in Figure 1, or even a combination of these.[23–25]

Such a wide structural variety however raises a fundamental concern, on how to efficiently discriminate among these different structures. How to quickly characterize, for instance, freshly synthesized compounds with a brand-new composition or samples containing phase mixtures? X-Ray Diffraction (XRD) is the spearhead technique to access the atomic structure of materials. It easily allows to confirm the formation of a target structure, given a reference diffraction pattern, and to fully resolve the atomistic crystalline structure of materials. Still, XRD provides information on long-range order and it may greatly benefit from other techniques with complementary features, notably those able to probe materials on a local scale. Within the stream of the so-called Nuclear Magnetic Resonance (NMR) crystallography, we propose here the Nuclear Quadrupolar Resonance (NQR), as an ideal technique to characterize new perovskite-derived materials, in particular, focusing on the chemical environment of the halides, which are actually involved in the most diverse chemical environment (different octahedral connectivity, dimensionalities, etc.). The inherently large nuclear quadrupolar moment of most abundant halides isotopes, in fact, which largely complicates their NMR response, is instead ideal for NQR spectroscopy.[26,27]

Tovborg-Jensen successfully exploited NQR to study phase transitions in $CsPbCl_3$,[28] observing the merging of two NQR signatures associated with the ^{35}Cl nuclei above 320 K temperature, consistently with the tetragonal→cubic phase transition previously reported by Møller.[29] Subsequent NQR studies by Van Vriel and Armstrong,[30] Plesko *et al.*[31] and by Hidaka *et al.*[32] allowed to propose specific space group sequences along the various temperature induced phase transitions and to highlight the presence of an additional one around 200 K.[32] Volkov *et al.*, instead focused on the ^{81}Br NQR measurements to investigate the phase diagram of $CsPbBr_3$, also reporting NQR signatures for the non-perovskite δ-phase of $CsPbI_3$.[33] NQR spectroscopy of bromine perovskites was later undertaken by Sharma *et al.*, who studied both $CsPbBr_3$ and $CsSnBr_3$.[34] Late eighties/early nineties witnessed the first NQR studies on hybrid, inorganic/organic perovskites, with Yamada *et al.* and Xu *et al.* performing NQR measurements of $MAGeCl_3$,[35] $MASnBr_3$,[36] and $MAPbX_3$ (X=Cl, Br, I),[37] (MA=methylammonium). An additional study by Asaij *et al.* focused on the NQR of ^{35}Cl nuclei in vacancy ordered HP phases, with different metal sites.[38] The interest in the use of NQR for the structural characterization of HPs re-kicked in these last years, following the arise of HP-based optoelectronic devices, with Franssen *et al.*,[39] and Senocrate *et al.*[40,41] exploiting NQR of ^{127}I to characterize the ion dynamics and defect mobility in $MAPbI_3$. The characterization of HPs via NQR measurements of the halides has been then expanded by Yamada *et al.*, who performed temperature-resolved ^{127}I NQR measurements of the black-phase of $FAPbI_3$ (FA=formamidinium) across the tetragonal→cubic phase transition, as well as of its non-perovskite δ-phase, at room temperature.[42]

This was followed by Piveteau *et al.* who reported the NQR characterization of $CsPbBr_3$ and $CsPbI_3$ HPs thin films and nanoparticles.[43,44] NQR spectroscopy also recently contributed to the intrinsically challenging characterization of HP with mixed compositions, namely, $FA_{1-x}Cs_xPbBr_3$ composition,[45] $FA_{1-x}Cs_XPbI_3$ (with x≤0.1) and $FAPb(I_{1-x}Br_x)_3$ (x≤0.04%).[46] Last but not least, the effect of additives on the structure and stability of 3D HP phases have also benefited from NQR measurements.[47–49]

NQR has however an important limitation, that is, the search for characteristic resonances may be difficult and extremely time-consuming. Typical frequency windows probed in one NQR measurement correspond in fact to around 1 kHz, at time, which makes the exploration of frequency domains of tens (for $^{35/37}Cl$) or hundreds (for $^{79/81}Br$ and ^{127}I) of MHz very demanding, at least in absence of any external indication. It comes very attractive therefore to have at least an initial guess of the expected spectral region, as from referring to an analogue compound with known NQR properties. Alternatively, the availability of parameter-free, first-principle simulations is emerging as a precious tool to obtain reasonable, informed guesses for the NQR frequencies.[45–49] Recently, Sarkar *et al.* performed DFT simulations in combination with NMR measurements of $^{35/37}Cl$ nuclei, to investigate the NQR properties of cesium chloride compounds with different metal sites, as well as lead-chloride compounds with different dimensionalities.[50] DFT-computed quadrupolar couplings properly paralleled the experimental results, supporting the finding that quadrupolar coupling itself can be related to the chloride-metal coordination number. This demonstrates that NQR is indeed directly informative of the atomic arrangement on a very local scale, discriminating between different types of octahedral connectivity. Very recently, Hooper *et al.* performed a combined theoretical/experimental study of the NQR properties of 3D, 2D and 0D lead-bromine compounds, once more demonstrating the strength of this synergic approach.[51]

Inspired by these findings, we report here a series of DFT calculations of the NQR response of ^{35}Cl, ^{81}Br and ^{127}I isotopes in various HPs and related compounds, covering a broad range of octahedra connectivities and dimensionalities (see Figure 1). Due to their technologic relevance,[1–9] we limit our investigations to lead-based compounds. For chlorine and bromine nuclei, we focus our study on most sensitive isotopes of each element, i.e. ^{35}Cl and ^{81}Br. Our results show that back-up from DFT calculations can greatly contribute to the NQR characterization of HP materials and related compounds. First, our DFT simulations show that NQR is able to discriminate the most diverse structures sketched in Figure 1. Second, theoretical calculations greatly support the interpretation of NQR signals, especially in the case when apparently small details are involved, as for the case of sites differing only in terms of local symmetry, rather than from dimensionality or connectivity. Third, with measurements probing only narrow frequency windows and requiring the long acquisition times, the experimental NQR activity may greatly benefit from an initial guess for the search of signals, which can be conveniently provided by DFT calculations. We close this investigation by reporting a roadmap of the characteristic frequencies associated with the NQR transitions of ^{127}I, for lead-iodide materials with different octahedral connectivity.

https://doi.org/10.1021/jacs.4c09877

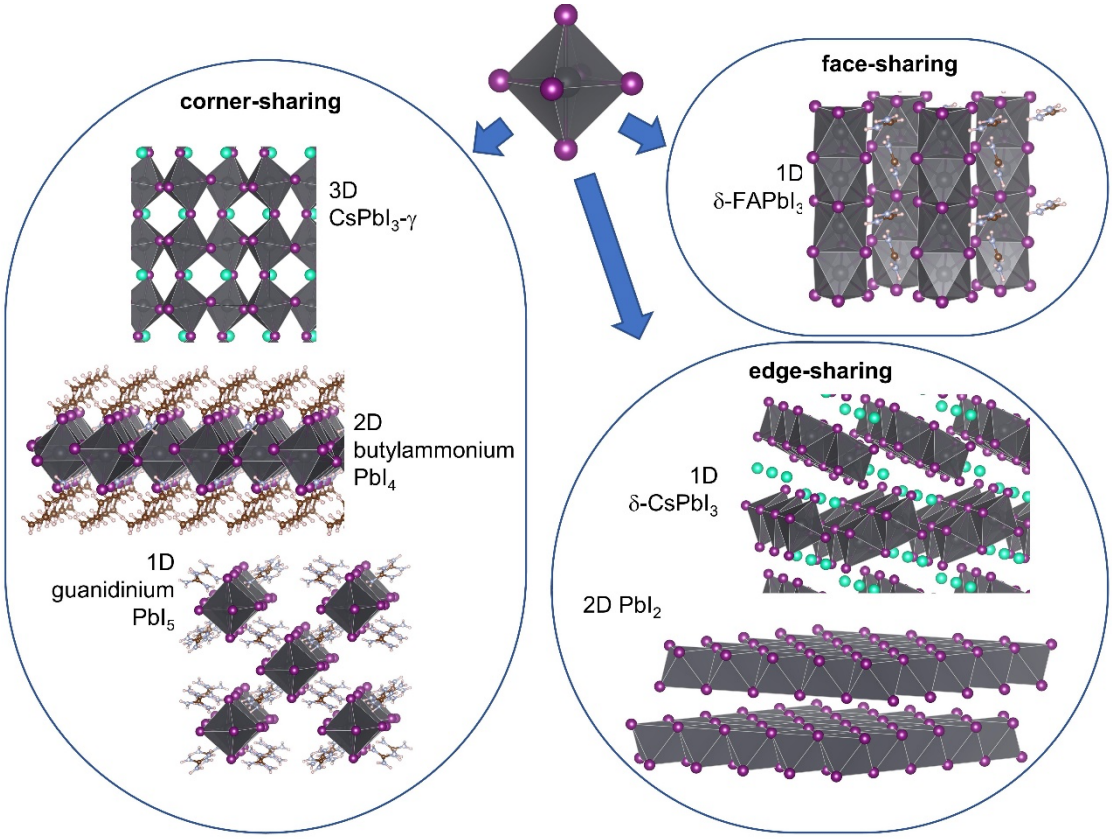

Figure 1. Examples of different organization of the PbX_6 octahedra (corner-, edge- and face-shared connectivity) and dimensionalities (3D, 2D, 1D and 0D) in perovskites and perovskitoids compounds.

Methods

The NQR comes from the interaction of the quadrupolar moment typical of nuclei with spin $I > ½$, with the Electric Field Gradient (EFG) imposed by the electronic cloud around the nucleus, which therefore carries information about its chemical environment. This interaction gives rise to a splitting of spin levels $|I, m_I\rangle$, which ultimately depends on two parameters, namely the quadrupolar coupling constant C_q and the anisotropy parameter η. A detailed mathematical treatment of the NQR interaction is reported in the Section 1 of the Supporting Information.[26,27]

For nuclei with spin I=3/2 (^{35}Cl, ^{79}Br and ^{81}Br), the quadrupolar interaction leads to only one signal, associated with two degenerate $|{}^3/_2, {}^1/_2\rangle \leftrightarrow |{}^3/_2, {}^3/_2\rangle$ and $|{}^3/_2, -{}^1/_2\rangle \leftrightarrow |{}^3/_2, -{}^3/_2\rangle$ transitions. It is therefore yet not possible to retrieve both C_q and η, with a single measurement. For nuclei with spin I=5/2 (^{127}I), the quadrupolar interaction leads to two signals associated with the transitions $\left|{}^5/_2, \pm {}^1/_2\right\rangle \leftrightarrow \left|{}^5/_2, \pm {}^3/_2\right\rangle$ and $\left|{}^5/_2, \pm {}^3/_2\right\rangle \leftrightarrow \left|{}^5/_2, \pm {}^5/_2\right\rangle$, which therefore allow to extract both the C_q and η. For spin I=5/2, we also highlight an important limit case, that nuclei characterized by an axially symmetric chemical environment (η=0) present the following relationship for the frequency (ν) of the two signals: $\nu_{\frac{3}{2}\leftrightarrow\frac{5}{2}} = 2\nu_{\frac{1}{2}\leftrightarrow\frac{3}{2}}$. This will be important for the discussion of some compounds.

The EFG tensor components are computed here using periodic DFT simulations, within the plane-wave/pseudopotential formalism, as implemented in the CASTEP suite code.[57–60] It is worth

mentioning that, though relatively unexploited for the case of halide perovskites, except for Ref.[50], the DFT simulation of the NQR properties of ^{127}I has been already exploited in the past.[61–63] For instance, a pioneering study devoted to EFG of solid iodine under pressure demonstrated that DFT calculations compare very well with experimental values determined by Mössbauer spectroscopy without taking into account spin-orbit interaction.[64] All the calculations reported in the main manuscript are based on the PBE functional to describe the exchange-correlation potential,[65] with relativistic effects included at the scalar relativistic level.

Spin orbit coupling (SOC) was shown to severely impact on the electronic properties of lead-based halide perovskites,[66] which motivated us to perform additional tests on its importance on the prediction of the NQR properties of these materials. Test calculations reported in the Section 2 of Supporting Information however showed that the inclusion of SOC along with standard PBE functional does not improve the agreement with respect to experiment, compared to the coarser scalar relativistic calculations. We speculate that such agreement from the formally less accurate approach is likely due to an error cancelation between lack of all electron treatment and relativistic spin orbit coupling, with the inaccurate treatment of electronic correlation with the employed PBE exchange-correlation functional.[67–69] It is also worth mentioning that these differences may be partly due to structural and motional effects, as the above NQR parameters refers to frozen models obtained from experimental XRD measurements. As a matter of fact previous studies showed that structural relaxation often plays a significant part in the computation of spectroscopic parameters.[70,71] More specifically, in metal halide perovskites, local disorder has been identified as a critical factor in accurately describing the electronic structure, vibrational dynamics, and optical properties of perovskite structures, significantly enhancing the agreement between theoretical predictions and experimental observations.[72–75] Based on this evidence, it is reasonable to assume that local disorder will significantly impact the electric field gradient at nuclear sites, and consequently, the NQR signal. To investigate this effect and account for local disorder we employed the anharmonic special displacement method,[74,76,77] as implemented in the EPW package,[78] for 3D perovskite frames. Details of the procedure for generating locally disordered structures and for the averaging of the NQR signals are reported in the Section 3 and 4 of the Supporting Information, respectively.

Results

NQR properties of 3D halide perovskites: site symmetry and revision of literature assignments

NQR was widely employed in the past to study phase transitions in 3D halide perovskites and related space group symmetries at various temperatures,[33,35–43,45–49] hence proving a solid ground for the validation of our computational set-up. Figure 2a reports the ^{35}Cl NQR frequency measured at room temperature on $CsPbCl_3$,[28] and $MAPbCl_3$,[37] while Figure 2b reports the ^{81}Br NQR frequency measured on $CsPbBr_3$,[34] and $MAPbBr_3$.[37] NQR frequencies are plotted against the corresponding lattice parameter, which here correspond to the experimental XRD reference at the closest temperature (Ref.[29] and Ref. [80], for the $CsPbX_3$ and $MAPbX_3$ (X=Cl, Br) compounds, respectively). Figure 2c-d show the two ^{127}I NQR frequencies associated with the $m_I = \frac{1}{2} \leftrightarrow \frac{3}{2}$ and $m_I = \frac{3}{2} \leftrightarrow \frac{5}{2}$ transitions, measured in $MAPbI_3$ at 350 K,[42] and in $FAPbI_3$ perovskite phase at room temperature,[42] along with the corresponding lattice parameters from Ref.[80] and Ref.[42]. At the experimental conditions in Refs.[28,34,37,42], all compounds are in their high-temperature pseudo-cubic phase, the change in the Cs/MA/FA component modulating the lattice parameter. Experimental findings in Figure 2 highlight an increase of the halide NQR frequencies, with increasing lattice parameter, further suggesting the potential role of NQR as a structural characterization tool in HP frames. Similar dependence was also

recently reported by Sarkar *et al.* for mixed-halide $CsPb(Br_xCl_{1-x})_3$ halide perovskites.[50] The experimental data are first compared with DFT estimates, obtained by considering highly symmetric (fixed *Pm-3m* space group) $CsPbX_3$. This model associates the change in frequency with the A component (Cs, MA, FA) solely with the corresponding change in the lattice parameter and it does not account for differences in the specific chemical interactions (hydrogen bonding between the A component and the PbX_3 lattice) nor for dynamic disorder. The corresponding theoretical results properly catch the frequency upshift with increasing the lattice parameter, though the upshift for Br-based and I-based compounds is underestimated. For the sake of reference, in iodide-based $MAPbI_3$/$FAPbI_3$ compounds, the frequency upshift with lattice parameter amounts only to 0.6/1.2 MHz, for the $m_I = \frac{1}{2} \leftrightarrow \frac{3}{2} / m_I = \frac{3}{2} \leftrightarrow \frac{5}{2}$ transitions, while the experimental upshift amounts to 4.3/8.6 MHz. In addition, compared to experiment, the NQR frequencies computed on this lattice-variable $CsPbX_3$-model are overestimated on average by 6.5%.

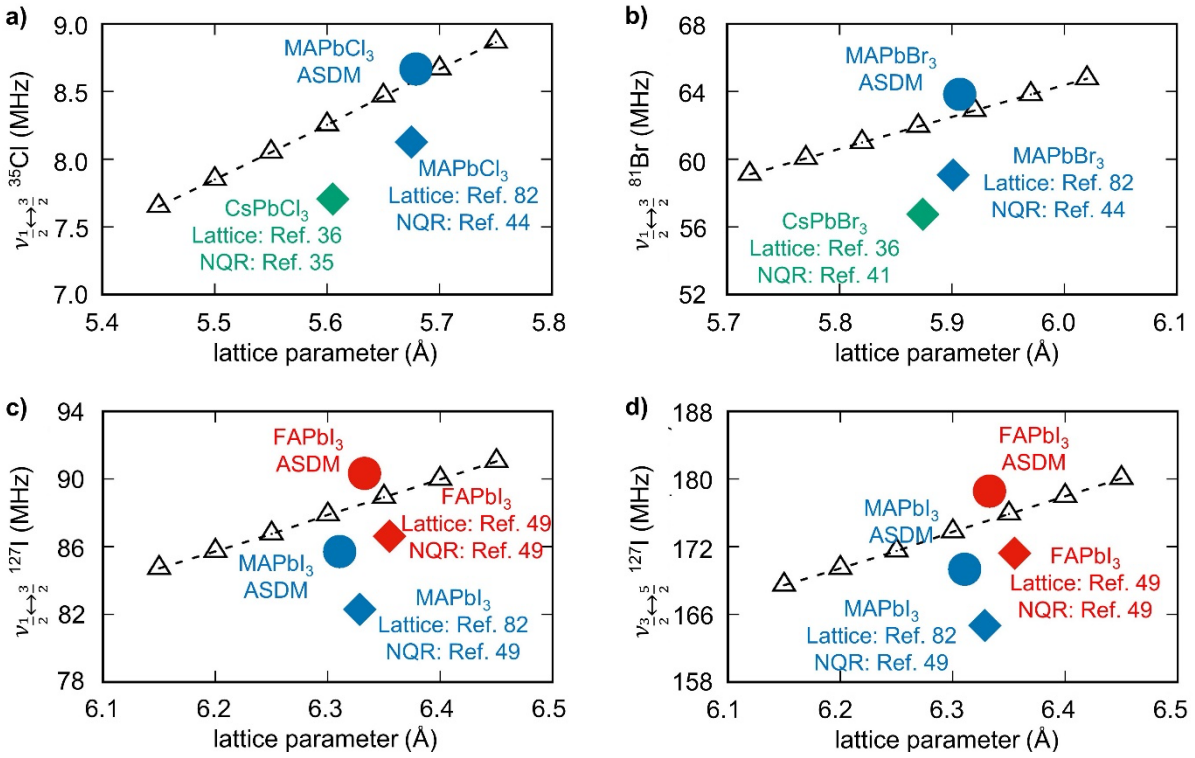

Figure 2. NQR frequencies versus cubic lattice parameter for (a) ^{35}Cl, (b) ^{81}Br and (c-d) ^{127}I nuclei, in 3D lead-halide perovskites. (diamond) Experimental data with perovskite composition and references relevant to the lattice parameter and to the NQR measurement. (triangles) High symmetry monomorphous cubic $CsPbX_3$ structure for different lattice constants. (circles) averaged values computed from 10 polymorphous structures determined from the anharmonic special displacement method (ASDM) including explicitly the organic cations.

Based on Figure 2, it is evident that the lattice modulation due to the Cs/FA/MA component is not sufficient to properly catch all the experimental features. On the other hand, the explicit inclusion of the FA/MA component in the simulation of the high temperature α-phase of halide perovskites is not a trivial task, as it undergoes to rapid (~ps) rotational dynamics.[71,72,81] It has recently been shown that this dynamic disorder can be approximated by static distortions using supercells designed with the anharmonic special displacement method (ASDM).[74,76,77] In practice, from the knowledge of the phonon band structure of a material together with geometry optimization, ASDM can construct a set

of representative quasi-static configurations that capture local disorder (polymorphous), representing energetically more stable configurations than high-symmetry (monomorphous) ones. We then computed the corresponding NQR properties and performed the correct average following the procedure described in the Section 4 of Supporting Information. The results in Figure 2 show that explicit inclusion of the organic component and dynamic disorder actually describes the frequency shifts from $MAPbI_3$ to $FAPbI_3$ to a far better extent (4.6/9.2 MHz), compared to the variable-lattice $CsPbI_3$ model. However, the theoretical frequencies computed including the role of the FA/MA cation are still overestimated, compared to the experiment, by 5.3% on average. Such discrepancy with experiment is not specific therefore to the procedure of Cs-substitution, but is related to the approximations of our DFT-based approach. At the opposite, the similar error obtained when applying the much simpler (and computationally less expensive) Cs-substitution indicates that this strategy is indeed a good proxy to perform a survey of a broad range of compounds, as targeted here.

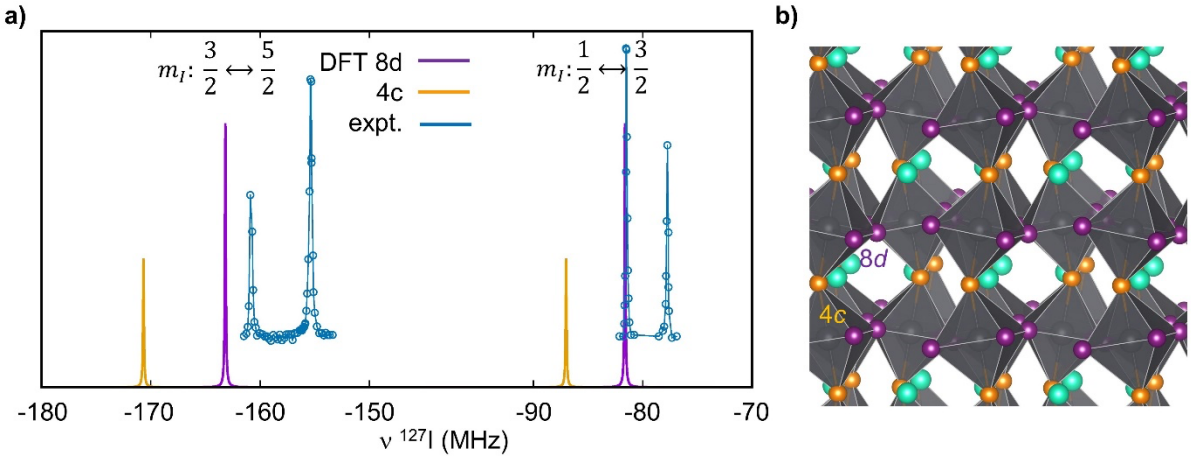

Figure 3. a) comparison of the experimental (blue line with dots) and DFT spectrum (purple and orange lines) for ^{127}I isotope in the γ-phase of $CsPbI_3$. The DFT spectrum distinguishes the signal from iodines sitting in the 4*c* (orange) and 8*d* (purple) Wyckoff positions of the HP lattice, which are illustrated in the panel **b)**. Experimental data in (a) reproduced from ACS Cent. Sci. 2020, 6, 1138−1149.[43] Copyright 2016 American Chemical Society.

We now pass to the orthorhombic γ-phase of $CsPbI_3$. Piveteau *et al.* recently measured the ^{127}I NQR signature of this phase, finding two doublets for each of the $m_I = \frac{1}{2} \leftrightarrow \frac{3}{2}$ and $m_I = \frac{3}{2} \leftrightarrow \frac{5}{2}$ transition, as shown in Figure 3a.[43] The observation of doublets in the NQR spectra of γ-$CsPbI_3$ is consistent with the presence of two different crystalline sites for the iodines, as in the crystalline model proposed by Marronnier *et al*. (*Pbnm* space group).[82] These can be conveniently classified based on the local site symmetry, namely as the 4*c* and 8*d* Wyckoff positions, illustrated in Figure 3b, which are sometimes referred in the literature as *apical* and *equatorial* halides.[83] Piveteau *et al.* therefore demonstrated the sensitivity of the NQR in discriminating between chemical environments differing in small details, such as the local site symmetry, but did not provide a clear assignment of the reported signals.[43] In this frame, our DFT calculations in Figure 3a allow to establish a detailed assignment, with the (absolute valued) lowest/highest component of each doublet associated with the 8*d*/4*c* Wyckoff site. In Section 5 of the Supporting Information, we report the survey of the NQR frequencies computed for all the three phases of $CsPbI_3$, using the monomorphous models reported in Ref. [82] (hence neglecting contributions from local disorder). The (absolute valued) signal associated

with the apical/equatorial iodides progressively downshifts/upshifts in frequency, when going from the orthorhombic, to the tetragonal phase of $CsPbI_3$, ultimately merging into a single signal in the cubic phase, consistently with the presence of only one crystalline site.

We extend the analysis to the γ-phase of halide perovskites to the Br-analog, $CsPbBr_3$. For this system, three different crystalline models have been reported in the literature, all belonging to the *Pbnm* space group (or to an equivalent set).[84–86] We hence performed DFT simulations for all of them (see Section 6 in the Supporting Information), finding only two signals, a first (second) between 63.0 and 65.1 (59.8 to 60.9) MHz, as function of the considered structural model. As before, our DFT calculations overestimate the NQR frequencies by few MHz but our results show that such discrepancy does also rely on the structural model considered. Apart from the numerical agreement, however, all models agree that the high frequency signal is associated with the 4c Wyckoff position and also open some question about previous experimental results. Original measurements in Ref.[33] reported in fact three NQR signals, at 55.78, 56.87 and 31.17 MHz (see also Table 2 of Ref. 32), which are not consistent with the presence of only two inequivalent sites for the bromines, in the lattice. A later work by Sharma et al.,[34] also confirmed the presence of the two high frequencies signatures but did not comment on the low frequency 31.17 MHz signal. We speculate that this low frequency signal is likely related to some impurity or secondary phase in the samples originally investigated in Ref.[33].

Interruption of the corner-sharing network and octahedral tilting in 2D HP

We move to discuss the impact of the interruption of the MX_6 corner-shared connectivity on the NQR properties of HPs, which is a very common perturbation of the prototypical perovskite structure and is at the core of the formation of 2D layered HPs. These compounds may be conceived as extended 2D sheets of corner-sharing MX_6 octahedra derived by slicing the reference cubic 3D perovskite structure along specific crystallographic planes, namely the <100>, <110> and <111> ones.[87] Reference models for <100>- and <110>-terminated 2D HPs are illustrated in Figure 4a. The interruption of the perovskite network leads to the definition of a new halide species, in addition to the corner-sharing halide discussed thus far, which *terminates* the perovskite lattice. Being chemically bound to only one metal site, the peculiar chemical environment of this terminal halide is expected to result also in specific NQR fingerprints but, to the best of our knowledge, no experimental measurements were reported thus far on this regard.[44] Indirect analyses of ^{35}Cl quadrupolar coupling from linewidth analyses of ^{35}Cl NMR measurements were only recently reported by Sarkar *et al.*, for various metal-chlorine compounds, but not involving the types of <100>- or <110>-terminated 2D structures, depicted in Figure 4a.[50] This motivates us to perform dedicated DFT simulations.

We hence designed hypothetical models of the <100>- and <110>-terminated models of 2D HP, with composition Cs_2PbX_4 and fixed P4mmm and Pmma space group symmetry, respectively (Figure 4a-b). For the <100>-terminated model, this leads to assigning the corner-shared and terminal iodines to the 2*f* and 2*g* Wyckoff positions, respectively, hence setting a one-to-one correspondence between the connectivity and the symmetry of the atomic site. For the <110>-model, such mapping is no longer possible, as the corner-shared halides belong either to 2*a* or 2*f* Wyckoff position, while the terminal iodine instead belongs solely to the 4*i* Wyckoff position. For a fair comparison with the corresponding results of the parental 3D HP phases, the initial structures of the 2D HP models in Figure 4a present all Pb-X distances equal to half the lattice parameter of the $MAPbX_3$ (X=Cl, Br, I), taken as common reference for all halides.[80] We then relaxed only the position of the terminal halide and cesium atoms and computed the NQR properties in Table 1. First focusing on the corner-sharing halide, we notice that for all 2D models, the NQR frequencies of this species in both the <100>- and

<110>-2D HP differ with respect to their 3D analogue. This suggests that the influence due to the dimensionality reduction on the NQR properties of 2D HP emerges already when analyzing the frequency window traditionally associated with the corner-sharing halide species. The NQR frequency difference between 3D and 2D structures increases going from Cl- to Br- and to I- based compounds, and from <100>- to <110>-terminated 2D lattice. With iodine-based compounds showing the largest 3D vs. 2D difference, these reveal the ideal bench-test for the experimental verification of our predictions. Apart from the frequency of the NQR transitions, it is also worth noticing that none of the corner-sharing halides experiences an axially symmetric environment, as also evident from their site symmetry in Table 1, leading to a breakdown of the condition $\nu_{\frac{3}{2}\leftrightarrow\frac{5}{2}} = 2\nu_{\frac{1}{2}\leftrightarrow\frac{3}{2}}$. The computed asymmetry parameter ranges from 0.03 to 0.28. Focusing instead on the most intriguing *terminal* halide, our DFT calculations suggest that this species indeed presents NQR transitions at a very specific frequency. The terminal halide in the <100>-frame, in particular, shows NQR transitions lying at half the frequency of their corner-shared analogues, as due to the much smaller quadrupolar couplings. With symmetry fixed to *P*4*mmm* space group, these species occupy a crystal site with axial symmetry, hence satisfying the condition $\nu_{\frac{3}{2}\leftrightarrow\frac{5}{2}} = 2\nu_{\frac{1}{2}\leftrightarrow\frac{3}{2}}$. Still, it is worth noticing that the terminal iodines from <100>- and <110>-2D HPs show considerably different NQR frequencies. This suggests therefore that similar metal-halide coordination number is not sufficient to lead to similar chemical environments, at least in terms of their NQR fingerprints.

Table 1. NQR frequencies for the various halides isotopes (^{35}Cl, ^{81}Br and ^{127}I) in <100>-terminated and <110>-terminated 2D HP Cs_2PbX_4 (X=Cl,Br, I) lattice models in Figure 4. These are compared with corresponding frequencies in the parental 3D HP cubic lattice. Halides are classified with respect to their Wyckoff Position (WP) and corresponding site symmetry.

Model	**WP**	**site symmetry**	**^{35}Cl**	**^{81}Br (MHz)**	**^{127}I**	
					m_I 1/2→3/2	**m_I 3/2→5/2**
			corner-shared			
3D	3*d*	*4mm*	8.57	63.15	88.48	176.95
2D-<100>	2*f*	*mmm*	8.82	64.74	84.23	153.32
2D-<110>	2*a*	*2/m*	7.51	56.77	74.82	148.48
	2*f*	*mm2*	7.76	57.96	80.40	160.55
			terminal			
2D-<100>	2*g*	*4mm*	3.89	29.01	41.30	82.61
2D-<110>	4*i*	*m*	6.53	45.36	52.44	89.17

Aiming to move towards more realistic structural details, we further dig into the influence of the octahedral tilting on the NQR properties of HPs. This is a very common type of distortion in perovskite frames,[88] and is known to influence the electronic properties of 2D HP compounds.[89–91] Using the distortion coordinates β and δ in Figure 4b, originally proposed by Pedesseau *et al.* to discriminate between in-plane and out-of-plane octahedral tilting,[89] we constructed progressively more distorted 2D HP models and computed the corresponding NQR properties. As the investigation of both Cl-, Br- and I-based 2D HP poses a significant computational hurdle, we limited to investigate only lead-iodine based compounds, also given their relevance for light-emission and photovoltaics. For all β and δ distortions, the Pb-I bond lengths are kept fixed to the reference values of the corresponding (undistorted) <100>-terminated in Figure 4a. Figure 4c reports the variation of the computed NQR frequency for the $m_I = \frac{1}{2} \leftrightarrow \frac{3}{2}$ transition, with respect to the reference undistorted case, both for the

corner-sharing and terminal iodines. For the corner-shared iodine, a combined 10/6 degrees out-of-plane/in-plane distortion downshifts the $m_I = \frac{1}{2} \leftrightarrow \frac{3}{2}$ transition frequency by 2 MHz. For the terminal iodine, the trend is reversed, with an increase of the NQR frequency with more distorted structures, up to 3MHz. As well as for the lead halide bond length, NQR frequencies are impacted by the degree of octahedral tilting.

We further consider the XRD model available for the widely investigated BA_2PbI_4 (BA=butylammonium) compound. We performed DFT calculations considering the static averaged structural model as available from XRD,[92] explicitly including the organic BA cation, and performing the Cs-substitution, as a cheap strategy to cope with dynamical disorder. Results in Figure S7 show that the frequencies computed following these two approaches are overall similar, with differences comprised between 1 and 6 MHz. The only exception is the $m_I = \frac{3}{2} \leftrightarrow \frac{5}{2}$ transition of the terminal iodines, where the difference is more evident (27 MHz). This stems essentially from the deviation from the axial symmetry of the chemical environment of terminal iodines, with the asymmetry parameter η amounting to 0.05 and 0.6 for Cs substituted and explicit cation, respectively. This change in the symmetry of the local environment reflects the presence of hydrogen bonding between the ammonium group of the BA spacers and the terminal iodines in the XRD structural data, which disappears upon Cs-substitution. Meanwhile, there is clear evidence from solid state NMR spectroscopy that the organic spacer are not fixed on the characteristic time of NQR measurements.[93,94] Besides, in lower dimensional perovskites, polymorphism similar to that evidenced in the cubic and tetragonal phases of 3D perovskites cannot be excluded. Unfortunately, implementation of a strategy combining ASDM and calculations of EFG tensor components is computationally very demanding and remains beyond the scope of the present work. Thus, in the absence of experimental NQR data it is difficult to state which of the two models is the most relevant. Still, all calculations in Figure 4 and S7 agree that the NQR frequency of terminal iodines in <100>-terminated 2D HP fall at lower frequencies (roughly half) than the equatorial ones that experience a corner-sharing chemical environment.

https://doi.org/10.1021/jacs.4c09877

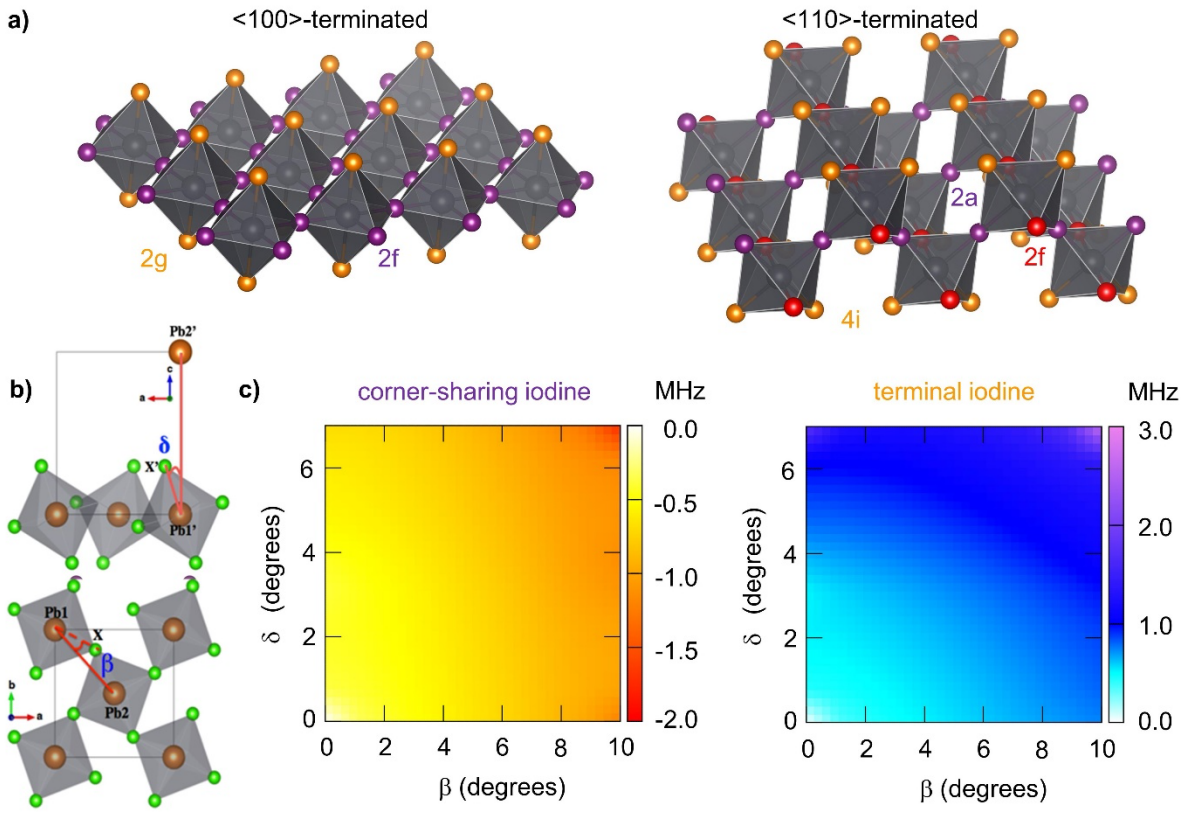

Figure 4. a) classification of the inequivalent halide positions in terms of crystalline sites, for hypothetical models of Cs_2PbX_4 <100>- and <110>-terminated 2D perovskite lattice; orange, purple and red spheres refer to the same halide, sitting in different crystalline Wyckoff position; **b)** definition of β- and δ- angles which define the octahedral tilting in a <100>-terminated, 2D halide perovskite lattice. Reproduced from J. Am. Chem. Soc. 2017, 139, 34, 11956–11963.[95] Copyright 2017 American Chemical Society; **c)** 2D map of the NQR resonance (MHz) for $m_I = \frac{1}{2} \leftrightarrow \frac{3}{2}$ transition for the corner sharing iodine and the terminal iodine in a <100>-terminated 2D halide perovskite lattice.

Next, we analyze the case of multi-*n* 2D lead-iodide HP compounds, which conceptually bridge the 2D and 3D cases. These heterostructures, illustrated in Figure 5a, correspond to 2D perovskites of variable thickness, with *n* expressing number of PbI_6 octahedra stacked along the thickness of the 2D inorganic sheet. Here, we focus again on the lead-iodide case and construct the hypothetical undistorted $Cs_2Cs'_{n-1}Pb_nI_{3n+1}$ models in Figure 5a (Cesium has been hidden for clarity), cutting an ideal 3D structure along the <100> plane, with same in-plane lattice parameter as $MAPbI_3$. All models are characterized by mirror symmetry, hence presenting 3, 4 and 5 inequivalent iodine sites for the n=2, 3 and 4 multi-*n* perovskites, respectively, indicated in Figure 5a using different colors. Each increase *n* of the layer thickness hence leads to the definition of a new halide specie, buried further away from the surface. We optimized the position of the outmost terminal iodine and cesium atoms, as in the *n*=1 <100>-terminated 2D HP in Figure 3a, then we calculated the NQR properties of the various multi-*n* 2D HP models. The frequencies associated with the $m_I = \frac{1}{2} \leftrightarrow \frac{3}{2}$ transition are mapped in Figure 5b for all the inequivalent iodides, the signals of the *n*=1 model corresponding to the two values in Table 1. Increasing *n*-thickness leads to a modulation of the NQR frequency from the terminal iodine, which actually saturates around 50 MHz already for *n*=2. In contrast, the NQR frequency from the corner-sharing halide is weakly influenced by the thickness of the inorganic frame. The *n*=2 case witnesses

the formation of a new iodine specie (the blue atoms in Figure 5a), connecting the two octahedra stacked along the thickness of the perovskite sheet. Though all Pb-I distances in the bulk are kept fixed, this new iodine species features a different NQR frequency. The signal from this iodine species is also modulated by the *n*-thickness of the inorganic frame but remains distinct also for larger *n* values, being separated by few MHz from the signals of the outmost corner-sharing iodines. The *n*=3 case again features the definition of a new iodine species (red atoms in Figure 5a) in the central MX_6 octahedra, whose signal now is less than 1 MHz far from the transition frequency computed for the 3D reference model. Also the n=4 case features a novel signal which is pretty close to the reference 3D model. Though Figure 5 suggests a potential use of NQR to characterize multi-*n* 2D HPs, its applicability may be actually more limited. Additional factors, such as octahedral rotations in Figure 4 and other structural distortions including dynamic disorder are expected to impact the NQR signals, leading to loss of resolution. Still, the signature from the terminal iodine can be a trustful probe to discriminate between *n*=1 phases from thicker ones, thanks to the large calculated shift (10 MHz) of this signature with thickness and its appearance in a region that does not present other signals.

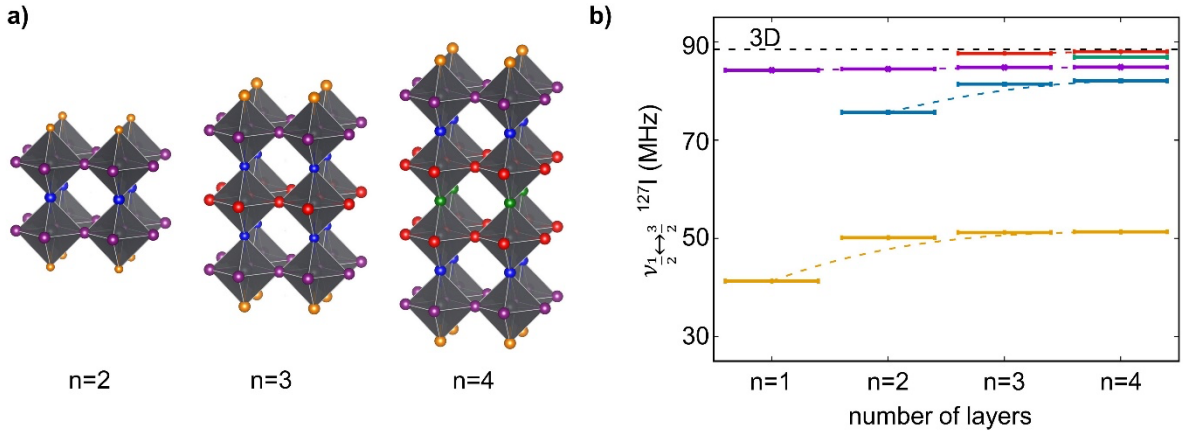

Figure 5. a) model structure for multi-n $Cs_2Cs'_{n-1}Pb_nI_{3n+1}$ (n=1,4) 2D lead-iodine perovskites (Cs atoms have been hidden, for the sake of simplicity). Inequivalent iodines are indicated with different colors; **b)** corresponding NQR resonance for the $m_I = \frac{1}{2} \leftrightarrow \frac{3}{2}$ transition.

NQR properties of face- and edge-sharing compounds

We extend this study by calculating the NQR properties of compounds characterized by octahedral connectivity other than corner-sharing, hence moving towards face-sharing and edge-sharing compounds. Two prototypical cases are represented by the yellow δ-phases of $FAPbI_3$ and $CsPbI_3$, which often appear as a result of degradation or as secondary phases from chemical synthesis of their perovskite analogues, and for whom the availability of an additional characterization tool may be technologically relevant. The δ-$FAPbI_3$ in Figure 6a is the prototypical case of a face-shared connectivity, the PbI_6 octahedra forming 1D stacks oriented along the high symmetry axis of the corresponding hexagonal cell. As for the case of $MAPbX_3$ and $FAPbX_3$ 3D HP, the hexagonal ($P6_3mc$) space group of δ-$FAPbI_3$ is inconsistent with the inherent C_{2v} symmetry of the FA molecule and results from the rapid rotational motion of the organic moiety, as discussed in Figure 2 for the α-phase of 3D halide perovskites. We hence proceeded to a similar substitution of the FA with Cs atoms, as done for 3D halide perovskites, as a cheap, yet appropriate procedure to cope with fast ionic motion, and performed DFT calculations. All iodines in the cell occupy the same Wyckoff 6*c* position, hence

showing the same transition frequencies at 55.22/82.37 MHz for the $m_I = \frac{1}{2} \leftrightarrow \frac{3}{2}$ /$m_I = \frac{3}{2} \leftrightarrow \frac{5}{2}$ transitions, nicely paralleling literature results (57.32/87.94 MHz).[42] Apart from numerical agreement, the downshift of both transitions compared to the 3D case is reproduced, together with the fact that the two frequencies approach each other, which is a sign of deviation from axial symmetry (see Figure S1) as reflected by the computed asymmetry parameter (η_Q around 0.5).

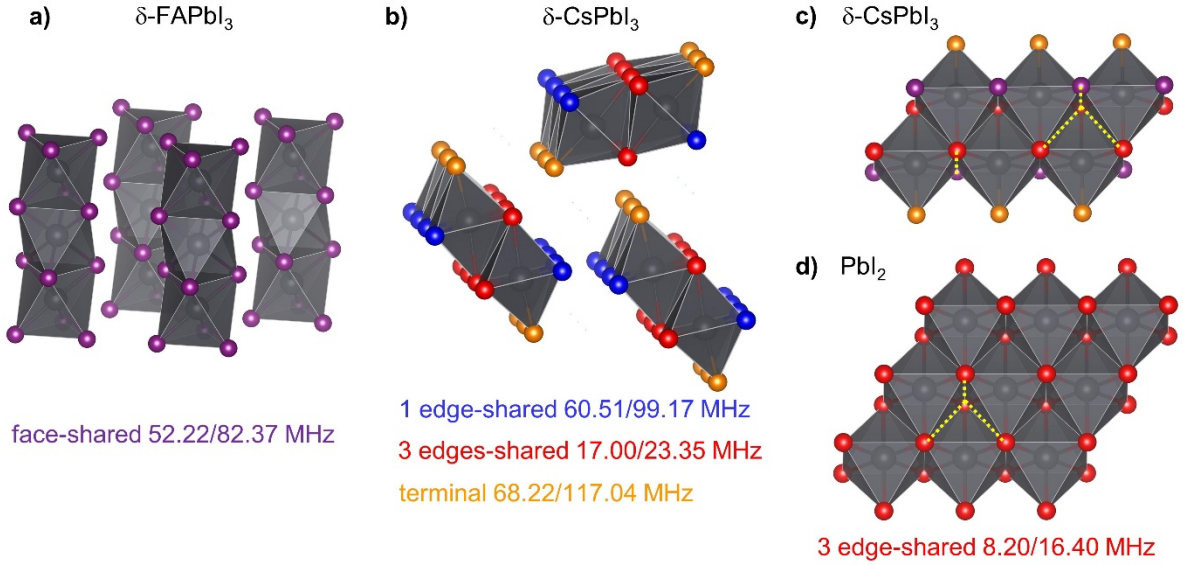

Figure 6. Structures for different non-corner-sharing lead-iodide perovskitoids, with corresponding $m_I = \frac{1}{2} \leftrightarrow \frac{3}{2}$/$m_I = \frac{3}{2} \leftrightarrow \frac{5}{2}$ NQR frequencies; **a)** 1D face-sharing, δ-phase of $FAPbI_3$; **b-c)** 1D edge-sharing, δ-phase of $CsPbI_3$; **d)** PbI_2. Symmetry inequivalent iodines are indicated using different colors.

The δ-phase of $CsPbI_3$ in Figure 6b is another case of practical interest since this is the most stable polymorph of $CsPbI_3$ in ambient conditions and parasite phases may appear in the preparation of the black perovskite phase. Its structure is characterized by edge-shared PbI_6 octahedra, packed along parallel 1D stacks, as from the reference XRD structure from Ref.[96]. Initial NQR investigations of this phase by Volkov *et al.* reported the presence of two pairs of signals at 70.15/125.2 MHz (signal #1) and 56.55/94.84 MHz (signal #2).[33] These signals have been recently confirmed by Piveteau *et al.*[43] and are routinely associated with the $m_I = \frac{1}{2} \leftrightarrow \frac{3}{2}$/$m_I = \frac{3}{2} \leftrightarrow \frac{5}{2}$ transitions of two iodines featuring different chemical environment. A closer glance to the crystal structure in Figure 6b, however, points out the presence of three symmetry inequivalent iodines, per unit cell, which should then result in three pairs of NQR signals. All three iodines lie in a different 4*c* Wyckoff position, hence making the site symmetry insufficient to individuate their chemical environments. It is however evident that one iodine lies in *terminal* position, as in 2D halide perovskites, being connected to only one metal site. The computed NQR frequencies of this iodine lie at 68.22/117.04 MHz, which is very close to the signal #1 found experimentally, falling at a frequency in between that of the corner-sharing and terminal halides in 2D lattices (see Table 1). Notice again that the characteristic NQR frequencies of this terminal iodine differ from those of both <100> and <110>-terminated 2D HP (Table 1), hence pointing out once more that the metal-halide coordination is not sufficient to fully characterize the chemical environment of the halides and to anticipate their NQR properties.

https://doi.org/10.1021/jacs.4c09877

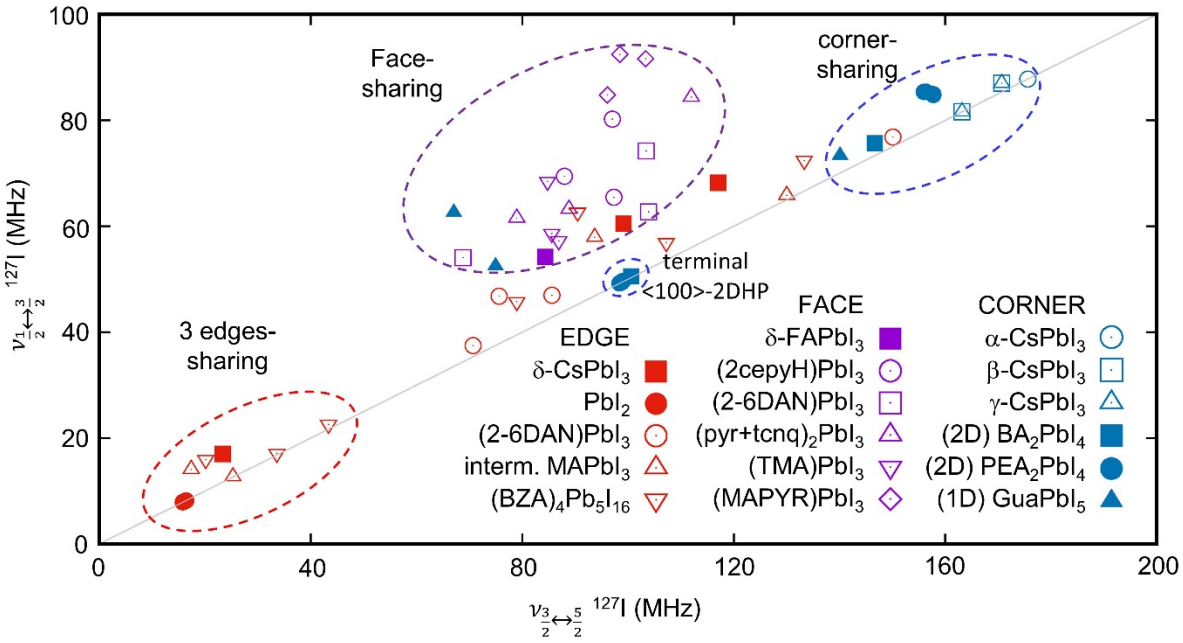

Figure 7. 2D map of the NQR frequencies for the $m_I = \frac{1}{2} \leftrightarrow \frac{3}{2}$ .vs. $m_I = \frac{3}{2} \leftrightarrow \frac{5}{2}$ transitions, as computed from DFT for various perovskite derivatives, classified based on the octahedral sharing pattern (corner/face/edge). Acronyms are the following: 2,6-DAN=2,6-diaminonaphthalene, interm. $MAPbI_3$=intermediate phase in $MAPbI_3$ formation; BZA=benzylammonium; 2cepyH=1-(2-chloroethyl)pyrrolidine); pyr+tcnq=pyrene+ tetracyanoquinodimethane; TMA=tetramethylammonium; MAPYR=4-methyl-1-aminopyridinium; BA=butylammonium; PEA=phenylethylammonium; Gua=guanidinium.

Dealing with the edge-sharing iodines, our calculations predict two pairs of transitions, consistently with the presence of two inequivalent edge-shared iodines species in the cell. The first transition pair sets at 60.51/99.17 MHz, in nice agreement with the signal #2 from Volkov *et al.*[33] The other is found at exceptionally low frequencies of 17.00/23.35 MHz . To the best of our knowledge, the corresponding signatures were not reported in the literature thus far. Although the big difference between these NQR frequencies is apparently surprising, given the same type of octahedral connectivity for these iodines, this becomes straightforward when noticing that these iodines actually do not share the same chemical environment. A closer glance to the crystal structure in fact reveals that while the iodine featuring high NQR frequency (60.51/99.17 MHz) is shared only between two PbI_6 octahedra, the iodine featuring low NQR frequency (17.00/23.35 MHz) is shared between three octahedra. Similarly, while the former iodine is surrounded by two metal sites (for distances < 3.5 Å), the latter is surrounded by three. To dig more into the NQR properties of edge-shared compounds, we performed additional DFT calculations on PbI_2. Apart from being a very common precursor for the preparation of lead-based HPs, this compound forms extended 2D edge-shared PbI_6 sheets, in contrast to the 1D stacks of δ-$CsPbI_3$, with all iodines being shared between three PbI_6 octahedra. Our DFT calculations confirm that the NQR frequency of this *three-edge* configuration lies at low 8.20/16.40 MHz frequency, also for PbI_2. For this compound, the chemical environment of iodines respects the condition in $\nu_{\frac{3}{2}\leftrightarrow\frac{5}{2}} = 2\nu_{\frac{1}{2}\leftrightarrow\frac{3}{2}}$, consistently with the C_3 axial site symmetry. To our knowledge, corresponding NQR frequencies have not been reported, yet, but an estimate of the quadrupolar constant ranging from 19 to 23 MHz was provided by Taylor *et al.* from the analysis of the NMR lineshapes, considering a perturbative treatment of the quadrupolar interactions. [97] This sets

the expected NQR frequencies between 2.9 and 3.5 MHz and between 5.7 and 6.9 MHz, for the $m_I = \frac{1}{2} \leftrightarrow \frac{3}{2}$ and the $m_I = \frac{3}{2} \leftrightarrow \frac{5}{2}$ transition, respectively. However, Piveteau *et al.* suggested that the use of perturbative treatment of the quadrupolar interaction is likely inappropriate for the ^{127}I nuclei,[43] hence casting some doubt about the accuracy of the experimental estimate in Ref. [97], reported without any confidence interval. Nevertheless, both DFT and experiment agree that the characteristic NQR frequency of these three-edge sharing iodines should lie at much lower frequencies than those reported for both corner- and edge-sharing iodines. This further supports the presence of a low-lying signal in the δ-phase of $CsPbI_3$.

To provide a bird's eye overview of our DFT results, we show in Figure 7 the frequencies computed for a range of lead-iodine compounds in shape of $\nu_{\frac{1}{2}\leftrightarrow\frac{3}{2}}$ against $\nu_{\frac{3}{2}\leftrightarrow\frac{5}{2}}$ map. The grey line represents the condition expressed in $\nu_{\frac{3}{2}\leftrightarrow\frac{5}{2}} = 2\nu_{\frac{1}{2}\leftrightarrow\frac{3}{2}}$, associated with an axially symmetric chemical environment. Aiming to build a roadmap to guide the experimental search of NQR signals, in Figure 7 we privileged compounds with experimentally resolved XRD structure, which equally cover corner-, edge- and face-sharing connectivity of the octahedra. Again, all organic moieties are substituted with Cs, the alkali atoms lying at the position of the nitrogen of the ammonium anchoring (except for FA, where cesium lies in place of the carbon), so to account for motional averaging and to stay consistent with the previous calculations. All corresponding C_Q and η_Q parameters, along with some reference results for lead-chlorine and lead-bromine compounds, are also listed in Table 2.

Though ^{127}I NQR frequencies in Figure 7 spread over a wide frequency domain (100 MHz/200 MHz, for $m_I = \frac{1}{2} \leftrightarrow \frac{3}{2}$ and $m_I = \frac{3}{2} \leftrightarrow \frac{5}{2}$, respectively), we can spot some peculiar trends associated with each specific PbI_6 octahedra connectivity. Compounds with corner-sharing connectivity all present NQR signals in the high frequency range, above 80 MHz/160 MHz for the $m_I = \frac{1}{2} \leftrightarrow \frac{3}{2}$ /$m_I = \frac{3}{2} \leftrightarrow \frac{5}{2}$, transition, respectively. This is not just the case of 3D networks but also of <100>-2D HPs and 1D compounds. The $GuaPbI_5$ case from Ref.[98], whose structure is depicted in Figure 1, is particularly enlightening in this concern. Presenting linear 1D chains of corner-shared octahedra running parallel each other, this compound has four terminal iodines for each PbI_6 octahedron. Still, the two remaining corner-shared iodines present NQR frequencies which lie just few MHz below those of the reference 3D corner-sharing, $CsPbI_3$ compound. It is also worth noting that the signals from corner-sharing PbI_6 octahedra lie close to the grey line, their chemical environment hence experiencing very small deviations from the axial symmetry ($\eta_Q \rightarrow 0$).

Table 2. List of computed C_Q and η_Q NQR parameters for a set of corner-, edge- and face-sharing HP and perovskitoid compounds. For each compound, experimental reference to the eventual experimental NQR datum and experimental crystal structure are indicated. In the latter case, the CCDC (C) and ISCD (I) reference number is also provided.

compound	experimental NQR				theoretical NQR		structure	
	$\|C_Q\|$ (MHz)	η_Q	ref	temp (K)	$\|C_Q\|$ (MHz)	η_Q	ref	temp (K)
corner-sharing								
α-$CsPbCl_3$					16.51	0.00	29	320
α-$MAPbCl_3$					17.13	0.00	80	179
α-$CsPbBr_3$					120.10	0.00	29	403
γ-$CsPbBr_3$					(4c) 125.88	0.04	85	298
					(8d) 121.84	0.01		
α-$MAPbBr_3$					127.14	0.00	80	237
α-$MAPI_3$	547.59	0.00	42	351	590.05	0.00	80	327
α-$FAPbI_3$	577.40	0.00	42	293	593.53	0.00	42	293
α-$CsPbI_3$					585.40	0.00	82	625
β-$CsPbI_3$					(2b) 585.7854	0.00	82	410
					(8i) 565.8853	0.01		
γ-$CsPbI_3$	517.98	0.03	43	293	(4c) 543.97	0.02	82	325
	537.36	0.10			(8d) 570.65	0.12		
BA_2PbI_4 (2D)					terminal (2i) 335.49	0.06	92	223
					(2f) 491.27	0.16		
$GuaPbI_5$ (1D)					470.46	0.19	98 1861695 C	298
					terminal 250.07	0.92		
					terminal 264.60	0.59		
edge-sharing								
δ-$CsPbI_3$	319.7	0.42	43	293	341.58	0.43	96 161480 I	298
	424.3	0.31			400.07	0.37		
					83.03	0.63		
PbI_2	19-23		97	250-345	54.73	0.00	99 1623998 C	293
(2,6-DAN)PbI_3					502.18	0.14	100 2210029 C	100
					289.65	0.28		
					261.16	0.44		
					237.83	0.22		
$MAPbI_3$					434.20	0.10	101	100
Intermediate					323.47	0.44		
phase					84.24	0.75		
					63.10	0.05		
$(BZA)_4Pb_5I_{16}$					112.21	0.12	102 1549803 C	100
$+H_2O$					145.40	0.18		
					269.65	0.36		
					72.69	0.73		
					318.82	0.58		
					360.87	0.22		
					450.37	0.26		
face-sharing								
δ-$FAPbI_3$	306.50	0.51	42	300	293.35	0.49	103 250741 I	293
(2cepyH)PbI_3					317.70-353.62	0.54-0.78	104 2094888 C	293
(2,6-DAN)PbI_3					366.90-248.20	0.62-0.72	100 2210030 C	100
(Pyr+TCNQ)PbI_3					400.85-284.49	0.67-0.71	105	100
(TMA)PbI_3					307.52-301.01	0.52-0.75	106	110
(MAPYR)PbI_3					354.52-381.65	0.85-0.92	107	293

NQR frequencies of face-sharing compounds also clusterize at intermediate frequencies between 60-90 MHz/60-100 MHz and lie considerably above the grey line, indicating a large deviation of their chemical environment from axial symmetry (all η_Q >0.49, see Table 2).

The case of edge-sharing compounds, at the end, is the most difficult to analyze. Our calculations in fact predict the widest dispersion of their ^{127}I NQR frequencies, reflecting the different chemical environments already partly discussed in Figure 6. Nevertheless, it is possible to associate the chemical environment of 3 octahedra-shared iodines with the low frequency (<25/<45 MHz) region. Also, for these 3 edge-sharing iodines, their NQR signals align close to the axial symmetry condition, this structural configuration being indeed associate with a local C_3 symmetry axis of the prototypical PbI_2 reference compound.

We further discuss the case of terminal iodines in <100>-terminated 2D HP, given the great interest around these compounds. Though we did not perform a systematic investigation over many 2D HPs , we find that the signals associated with the termina iodides of the reference BA_2PbI_4 2D HP localize in a very specific frequency window, separated from that of the other iodine species. As a final notice, we already pointed out that our DFT set-up overestimates the NQR frequencies for halides in HP and perovskitoids by few %. Such overestimation may originate from molecular motion (e.g. rotational dynamics and structural averaging due to thermal effects), as well as from an unbalanced error cancelation between electronic correlation and spin-orbit interaction, or even from a combination of all these effects. Still, it is important for experimentalists to account for such overestimate, when searching for specific NQR signals in their measurements.

Conclusions

In this work, we investigate the possibility of exploiting NQR spectroscopy of halide isotopes for the characterization of HPs and analogous perovskitoid compounds. Based on parameter-free, periodic DFT simulations, we computed the halide NQR properties in a wide set of lead-halide perovskite and perovskitoid compounds, with a special focus on lead-iodide compositions, considering the different connectivity of the PbI_6 octahedra (corner-, face- and edge-sharing) as well as various lattice dimensionalities. Our calculations nicely fit the few available experimental results. More, they anticipate that distinctive NQR frequency ranges can be associated to edge-, face- and corner-sharing as well as to terminal halide sites. This is particularly useful to assess the local octahedral connectivity but also to identify the presence of impurity phases. Finally, our results afford a set of informed guesses for the characteristic frequencies of various iodide perovskites and perovskitoids that will enable to significantly narrow down the experimental frequency range to explore.

From an experimental point of view, it would be valuable to assess these predictions, with for instance the technologically relevant (multi)-layered perovskites and more specifically the terminal versus equatorial iodine nuclei. On the theory side, we clearly showed that the structural model used has a dramatic impact on the computed EFG tensor components and in turn on the frequencies and asymmetry parameter, which need a correct procedure for averaging. In particular, we demonstrate the importance to account for the local disorder (polymorphism according to A. Zunger)[73] for the cubic halide perovskites and further work in this direction is desirable for other structural arrangements. Meanwhile, we show that substitution of the organic molecule with a Cesium provides a reasonable first approximation to account for the dynamical disorder that takes place. Noteworthy, besides investigation of the impact of structural models, our work did not assess the various sources of broadening that may limit the signal to noise ratio in experiment. Such broadening may be particularly important in mixed compositions with cation and/or halide and/or metal alloying.[45,46]

Acknowledgements

The authors warmly thank Prof. Jacky Even for useful and constructive discussions. The work at ISCR was supported by the Agence Nationale pour la Recherche (MORELESS project). M.Z. acknowledges funding by the European Union (project ULTRA-2DPK / HORIZON-MSCA-2022-PF-01 / Grant Agreement No. 101106654). Views and opinions expressed are however those of the authors only and do not necessarily reflect those of the European Union or the European Commission. Neither the European Union nor the granting authority can be held responsible for them. For DFT calculations, this work was granted access to the HPC resources of TGCC/CINES/IDRIS under the allocation 2020-A0090907682 made by GENCI. Computational resources have been also provided by the Consortium des Équipements de Calcul Intensif (CÉCI), funded by the Fonds de la Recherche Scientifique de Belgique (F.R.S.-FNRS) under Grant No. 2.5020.11 and by the Walloon Region. C.Q. is an FNRS research associate. We also acknowledge computational resources from the EuroHPC Joint Undertaking and supercomputer LUMI [https://lumi-supercomputer.eu/], hosted by CSC (Finland) and the LUMI consortium through a EuroHPC Extreme Scale Access call.

Supporting Information

Detailed mathematical treatment of the NQR interaction and NQR Hamiltonian for spin 3/2 and 5/2; Computational details for the DFT simulations and results of the convergence tests; Generation of locally disordered (polymorphous) structures; Procedure for averaging the NQR properties of a compound from an ensemble of representative structural models; NQR frequencies computed for the orthorhombic (γ-), tetragonal (β-) and (pseudo-)cubic (α-)phase of $CsPbI_3$ perovskite; NQR frequencies computed for the γ-phase of $CsPbBr_3$ perovskite; NQR frequencies of BA_2PbI_4 with explicit organic spacer and Cs-substitution

References

(1) Aydin, E.; Allen, T. G.; De Bastiani, M.; Razzaq, A.; Xu, L.; Ugur, E.; Liu, J.; De Wolf, S. Pathways toward Commercial Perovskite/Silicon Tandem Photovoltaics. *Science* **2024**, *383* (6679), eadh3849. https://doi.org/10.1126/science.adh3849.

(2) Chen, H.; Liu, C.; Xu, J.; Maxwell, A.; Zhou, W.; Yang, Y.; Zhou, Q.; Bati, A. S. R.; Wan, H.; Wang, Z.; Zeng, L.; Wang, J.; Serles, P.; Liu, Y.; Teale, S.; Liu, Y.; Saidaminov, M. I.; Li, M.; Rolston, N.; Hoogland, S.; Filleter, T.; Kanatzidis, M. G.; Chen, B.; Ning, Z.; Sargent, E. H. Improved Charge Extraction in Inverted Perovskite Solar Cells with Dual-Site-Binding Ligands. *Science* **2024**, *384* (6692), 189–193. https://doi.org/10.1126/science.adm9474.

(3) Kumar, S.; Jagielski, J.; Yakunin, S.; Rice, P.; Chiu, Y.-C.; Wang, M.; Nedelcu, G.; Kim, Y.; Lin, S.; Santos, E. J. G.; Kovalenko, M. V.; Shih, C.-J. Efficient Blue Electroluminescence Using Quantum-Confined Two-Dimensional Perovskites. *ACS Nano* **2016**, *10* (10), 9720–9729. https://doi.org/10.1021/acsnano.6b05775.

(4) Yang, R.; Li, R.; Cao, Y.; Wei, Y.; Miao, Y.; Tan, W. L.; Jiao, X.; Chen, H.; Zhang, L.; Chen, Q.; Zhang, H.; Zou, W.; Wang, Y.; Yang, M.; Yi, C.; Wang, N.; Gao, F.; McNeill, C. R.; Qin, T.; Wang, J.; Huang, W. Oriented Quasi-2D Perovskites for High Performance Optoelectronic Devices. *Advanced Materials* **2018**, *30* (51), 1804771. https://doi.org/10.1002/adma.201804771.

(5) Tsai, H.; Nie, W.; Blancon, J.-C.; Stoumpos, C. C.; Soe, C. M. M.; Yoo, J.; Crochet, J.; Tretiak, S.; Even, J.; Sadhanala, A.; Azzellino, G.; Brenes, R.; Ajayan, P. M.; Bulović, V.; Stranks, S. D.; Friend, R. H.; Kanatzidis, M. G.; Mohite, A. D. Stable Light-Emitting Diodes Using Phase-Pure Ruddlesden–Popper Layered Perovskites. *Advanced Materials* **2018**, *30* (6), 1704217. https://doi.org/10.1002/adma.201704217.

(6) Tsai, H.; Nie, W.; Blancon, J.-C.; Stoumpos, C. C.; Asadpour, R.; Harutyunyan, B.; Neukirch, A. J.; Verduzco, R.; Crochet, J. J.; Tretiak, S.; Pedesseau, L.; Even, J.; Alam, M. A.; Gupta, G.; Lou, J.; Ajayan, P. M.; Bedzyk, M. J.; Kanatzidis, M. G.; Mohite, A. D. High-Efficiency Two-Dimensional Ruddlesden–Popper Perovskite Solar Cells. *Nature* **2016**, *536* (7616), 312–316. https://doi.org/10.1038/nature18306.

(7) Liang, C.; Gu, H.; Xia, Y.; Wang, Z.; Liu, X.; Xia, J.; Zuo, S.; Hu, Y.; Gao, X.; Hui, W.; Chao, L.; Niu, T.; Fang, M.; Lu, H.; Dong, H.; Yu, H.; Chen, S.; Ran, X.; Song, L.; Li, B.; Zhang, J.; Peng, Y.; Shao, G.; Wang, J.; Chen, Y.; Xing, G.; Huang, W. Two-Dimensional Ruddlesden–Popper Layered Perovskite Solar Cells Based on Phase-Pure Thin Films. *Nat Energy* **2021**, *6* (1), 38–45. https://doi.org/10.1038/s41560-020-00721-5.

(8) Sun, C.; Jiang, Y.; Cui, M.; Qiao, L.; Wei, J.; Huang, Y.; Zhang, L.; He, T.; Li, S.; Hsu, H.-Y.; Qin, C.; Long, R.; Yuan, M. High-Performance Large-Area Quasi-2D Perovskite Light-Emitting Diodes. *Nat Commun* **2021**, *12* (1), 2207. https://doi.org/10.1038/s41467-021-22529-x.

(9) Yuan, S.; Wang, Z.-K.; Xiao, L.-X.; Zhang, C.-F.; Yang, S.-Y.; Chen, B.-B.; Ge, H.-T.; Tian, Q.-S.; Jin, Y.; Liao, L.-S. Optimization of Low-Dimensional Components of Quasi-2D Perovskite Films for Deep-Blue Light-Emitting Diodes. *Advanced Materials* **2019**, *31* (44), 1904319. https://doi.org/10.1002/adma.201904319.

(10) Sidhik, S.; Wang, Y.; De Siena, M.; Asadpour, R.; Torma, A. J.; Terlier, T.; Ho, K.; Li, W.; Puthirath, A. B.; Shuai, X.; Agrawal, A.; Traore, B.; Jones, M.; Giridharagopal, R.; Ajayan, P. M.; Strzalka, J.; Ginger, D. S.; Katan, C.; Alam, M. A.; Even, J.; Kanatzidis, M. G.; Mohite, A. D. Deterministic Fabrication of 3D/2D Perovskite Bilayer Stacks for Durable and Efficient Solar Cells. *Science* **2022**, *377* (6613), 1425–1430. https://doi.org/10.1126/science.abq7652.

(11) Degani, M.; An, Q.; Albaladejo-Siguan, M.; Hofstetter, Y. J.; Cho, C.; Paulus, F.; Grancini, G.; Vaynzof, Y. 23.7% Efficient Inverted Perovskite Solar Cells by Dual Interfacial Modification. *Science Advances* **2021**, *7* (49), eabj7930. https://doi.org/10.1126/sciadv.abj7930.

(12) De Wolf, S.; Holovsky, J.; Moon, S.-J.; Löper, P.; Niesen, B.; Ledinsky, M.; Haug, F.-J.; Yum, J.-H.; Ballif, C. Organometallic Halide Perovskites: Sharp Optical Absorption Edge and Its Relation to Photovoltaic Performance. *J. Phys. Chem. Lett.* **2014**, *5* (6), 1035–1039. https://doi.org/10.1021/jz500279b.

(13) Noh, J. H.; Im, S. H.; Heo, J. H.; Mandal, T. N.; Seok, S. I. Chemical Management for Colorful, Efficient, and Stable Inorganic–Organic Hybrid Nanostructured Solar Cells. *Nano Lett.* **2013**, *13* (4), 1764–1769. https://doi.org/10.1021/nl400349b.

(14) Mosconi, E.; Umari, P.; Angelis, F. D. Electronic and Optical Properties of MAPbX3 Perovskites (X = I, Br, Cl): A Unified DFT and GW Theoretical Analysis. *Phys. Chem. Chem. Phys.* **2016**, *18* (39), 27158–27164. https://doi.org/10.1039/C6CP03969C.

(15) Wehrenfennig, C.; Eperon, G. E.; Johnston, M. B.; Snaith, H. J.; Herz, L. M. High Charge Carrier Mobilities and Lifetimes in Organolead Trihalide Perovskites. *Advanced Materials* **2014**, *26* (10), 1584–1589. https://doi.org/10.1002/adma.201305172.

(16) Xing, G.; Mathews, N.; Sun, S.; Lim, S. S.; Lam, Y. M.; Grätzel, M.; Mhaisalkar, S.; Sum, T. C. Long-Range Balanced Electron- and Hole-Transport Lengths in Organic-Inorganic CH3NH3PbI3. *Science* **2013**, *342* (6156), 344–347. https://doi.org/10.1126/science.1243167.

(17) Stranks, S. D.; Eperon, G. E.; Grancini, G.; Menelaou, C.; Alcocer, M. J. P.; Leijtens, T.; Herz, L. M.; Petrozza, A.; Snaith, H. J. Electron-Hole Diffusion Lengths Exceeding 1 Micrometer in an Organometal Trihalide Perovskite Absorber. *Science* **2013**, *342* (6156), 341–344. https://doi.org/10.1126/science.1243982.

(18) Yuan, Z.; Zhou, C.; Tian, Y.; Shu, Y.; Messier, J.; Wang, J. C.; van de Burgt, L. J.; Kountouriotis, K.; Xin, Y.; Holt, E.; Schanze, K.; Clark, R.; Siegrist, T.; Ma, B. One-Dimensional Organic Lead Halide Perovskites with Efficient Bluish White-Light Emission. *Nat Commun* **2017**, *8* (1), 14051. https://doi.org/10.1038/ncomms14051.

(19) Zhang, B.-B.; Liu, X.; Xiao, B.; Hafsia, A. B.; Gao, K.; Xu, Y.; Zhou, J.; Chen, Y. High-Performance X-Ray Detection Based on One-Dimensional Inorganic Halide Perovskite CsPbI3. *J. Phys. Chem. Lett.* **2020**, *11* (2), 432–437. https://doi.org/10.1021/acs.jpclett.9b03523.
(20) Yang, X.; Ma, L.-F.; Yan, D. Facile Synthesis of 1D Organic–Inorganic Perovskite Micro-Belts with High Water Stability for Sensing and Photonic Applications. *Chemical Science* **2019**, *10* (17), 4567–4572. https://doi.org/10.1039/C9SC00162J.
(21) Wang, J.; Yang, J.-H.; Chen, J.; Wang, S.-H.; Chen, Y.-J.; Xu, G. 1D Pb Halide Perovskite-like Materials for High Performance X-Ray Detection. *Chem. Commun.* **2024**, *60* (24), 3311–3314. https://doi.org/10.1039/D4CC00510D.
(22) Diez-Cabanes, V.; Giannini, S.; Beljonne, D.; Quarti, C. On the Origin of Energetic Disorder in Mixed Halides Lead Perovskites. *Advanced Optical Materials* **2023**. https://doi.org/10.1002/adom.202301105.
(23) Kamminga, M. E.; Fang, H.-H.; Filip, M. R.; Giustino, F.; Baas, J.; Blake, G. R.; Loi, M. A.; Palstra, T. T. M. Confinement Effects in Low-Dimensional Lead Iodide Perovskite Hybrids. *Chem. Mater.* **2016**, *28* (13), 4554–4562. https://doi.org/10.1021/acs.chemmater.6b00809.
(24) Tian, J.; Cordes, D. B.; Quarti, C.; Beljonne, D.; Slawin, A. M. Z.; Zysman-Colman, E.; Morrison, F. D. Stable 6H Organic–Inorganic Hybrid Lead Perovskite and Competitive Formation of 6H and 3C Perovskite Structure with Mixed A Cations. *ACS Appl. Energy Mater.* **2019**, *2* (8), 5427–5437. https://doi.org/10.1021/acsaem.9b00419.
(25) Li, X.; Kepenekian, M.; Li, L.; Dong, H.; Stoumpos, C. C.; Seshadri, R.; Katan, C.; Guo, P.; Even, J.; Kanatzidis, M. G. Tolerance Factor for Stabilizing 3D Hybrid Halide Perovskitoids Using Linear Diammonium Cations. *J. Am. Chem. Soc.* **2022**, *144* (9), 3902–3912. https://doi.org/10.1021/jacs.1c11803.
(26) Suits, B. H. NUCLEAR QUADRUPOLE RESONANCE SPECTROSCOPY. In *Handbook of Applied Solid State Spectroscopy*; Vij, D. R., Ed.; Springer US: Boston, MA, 2006; pp 65–96. https://doi.org/10.1007/0-387-37590-2_2.
(27) Das, T. P.; Hann, E. L. *Nuclear Quadrupole Resonance Spectroscopy*; Academic Press, NY, 1958.
(28) Tovborg-Jensen, N. NQR Investigation of Phase Transitions in Cesium Plumbochloride. *The Journal of Chemical Physics* **2003**, *50* (1), 559–560. https://doi.org/10.1063/1.1670853.
(29) Møller, C. K. Crystal Structure and Photoconductivity of Cæsium Plumbohalides. *Nature* **1958**, *182* (4647), 1436–1436. https://doi.org/10.1038/1821436a0.
(30) van Driel, H. M.; Armstrong, R. L. $^{35}\mathrm{Cl}$ Spin-Lattice Relaxation Study of Phase Transitions in CsPb${\mathrm{Cl}}_{3}$. *Phys. Rev. B* **1975**, *12* (3), 839–841. https://doi.org/10.1103/PhysRevB.12.839.
(31) Plesko, S.; Kind, R.; Roos, J. Structural Phase Transitions in CsPbCl3 and RbCdCl3. *J. Phys. Soc. Jpn.* **1978**, *45* (2), 553–557. https://doi.org/10.1143/JPSJ.45.553.
(32) Hidaka, M.; Okamoto, Y.; Zikumaru, Y. Structural Phase Transition of CsPbCl3 below Room Temperature. *physica status solidi (a)* **1983**, *79* (1), 263–269. https://doi.org/10.1002/pssa.2210790129.
(33) Volkov, A. F.; Venevtsev, Yu. N.; Semin, G. K. Nuclear Quadrupole Resonance (NQR) of 79Br and 81Br in Perovskite and Orthorhombic Forms of CsPbBr3 and CsPbJ3. *physica status solidi (b)* **1969**, *35* (2), K167–K169. https://doi.org/10.1002/pssb.19690350277.
(34) Sharma, S.; Weiden, N.; Weiss, A. Phase Transitions in CsSnCl3 and CsPbBr3 An NMR and NQR Study. *Zeitschrift für Naturforschung A* **1991**, *46* (4), 329–336. https://doi.org/10.1515/zna-1991-0406.
(35) Yamada, K.; Mikawa, K.; Okuda, T.; Knight, K. S. Static and Dynamic Structures of CD3ND3GeCl3 Studied by TOF High Resolution Neutron Powder Diffraction and Solid State NMR. *J. Chem. Soc., Dalton Trans.* **2002**, No. 10, 2112–2118. https://doi.org/10.1039/B201611G.

(36) Yamada, K.; Nose, S.; Umehara, T.; Okuda, T.; Ichiba, S. 81Br NQR and 119Sn Mössbauer Study for MSnBr3 (M=Cs and CH3NH3). *BCSJ* **1988**, *61* (12), 4265–4268. https://doi.org/10.1246/bcsj.61.4265.

(37) Xu, Q.; Eguchi, T.; Nakayama, H.; Nakamura, N.; Kishita, M. Molecular Motions and Phase Transitions in Solid CH3NH3PbX3 (X = C1, Br, I) as Studied by NMR and NQR. *Zeitschrift für Naturforschung A* **1991**, *46* (3), 240–246. https://doi.org/10.1515/zna-1991-0305.

(38) Asaji, T.; Kume, Y.; Ohya, K.; Chiba, T. Structural Phase Transitions in Deuterated Ammonium Hexachloroplumbate(IV), , Studied by Nuclear Quadrupole Resonance. *J. Phys.: Condens. Matter* **1997**, *9* (12), 2563. https://doi.org/10.1088/0953-8984/9/12/005.

(39) Franssen, W. M. J.; Van Es, S. G. D.; Dervişoğlu, R.; De Wijs, G. A.; Kentgens, A. P. M. Symmetry, Dynamics, and Defects in Methylammonium Lead Halide Perovskites. *J. Phys. Chem. Lett.* **2017**, *8* (1), 61–66. https://doi.org/10.1021/acs.jpclett.6b02542.

(40) Senocrate, A.; Moudrakovski, I.; Kim, G. Y.; Yang, T.-Y.; Gregori, G.; Grätzel, M.; Maier, J. The Nature of Ion Conduction in Methylammonium Lead Iodide: A Multimethod Approach. *Angewandte Chemie International Edition* **2017**, *56* (27), 7755–7759. https://doi.org/10.1002/anie.201701724.

(41) Senocrate, A.; Moudrakovski, I.; Maier, J. Short-Range Ion Dynamics in Methylammonium Lead Iodide by Multinuclear Solid State NMR and ^{127}I NQR. *Phys. Chem. Chem. Phys.* **2018**, *20* (30), 20043–20055. https://doi.org/10.1039/C8CP01535J.

(42) Yamada, K.; Hino, S.; Hirose, S.; Yamane, Y.; Turkevych, I.; Urano, T.; Tomiyasu, H.; Yamagishi, H.; Aramaki, S. Static and Dynamic Structures of Perovskite Halides ABX3 (B = Pb, Sn) and Their Characteristic Semiconducting Properties by a Hückel Analytical Calculation. *Bulletin of the Chemical Society of Japan* **2018**, *91* (8), 1196–1204. https://doi.org/10.1246/bcsj.20180068.

(43) Piveteau, L.; Aebli, M.; Yazdani, N.; Millen, M.; Korosec, L.; Krieg, F.; Benin, B. M.; Morad, V.; Piveteau, C.; Shiroka, T.; Comas-Vives, A.; Copéret, C.; Lindenberg, A. M.; Wood, V.; Verel, R.; Kovalenko, M. V. Bulk and Nanocrystalline Cesium Lead-Halide Perovskites as Seen by Halide Magnetic Resonance. *ACS Cent. Sci.* **2020**, *6* (7), 1138–1149. https://doi.org/10.1021/acscentsci.0c00587.

(44) Piveteau, L.; Morad, V.; Kovalenko, M. V. Solid-State NMR and NQR Spectroscopy of Lead-Halide Perovskite Materials. *J. Am. Chem. Soc.* **2020**, *142* (46), 19413–19437. https://doi.org/10.1021/jacs.0c07338.

(45) Mozur, E. M.; Hope, M. A.; Trowbridge, J. C.; Halat, D. M.; Daemen, L. L.; Maughan, A. E.; Prisk, T. R.; Grey, C. P.; Neilson, J. R. Cesium Substitution Disrupts Concerted Cation Dynamics in Formamidinium Hybrid Perovskites. *Chem. Mater.* **2020**, *32* (14), 6266–6277. https://doi.org/10.1021/acs.chemmater.0c01862.

(46) Aebli, M.; Porenta, N.; Aregger, N.; Kovalenko, M. V. Local Structure of Multinary Hybrid Lead Halide Perovskites Investigated by Nuclear Quadrupole Resonance Spectroscopy. *Chem. Mater.* **2021**, *33* (17), 6965–6973. https://doi.org/10.1021/acs.chemmater.1c01945.

(47) Doherty, T. A. S.; Nagane, S.; Kubicki, D. J.; Jung, Y.-K.; Johnstone, D. N.; Iqbal, A. N.; Guo, D.; Frohna, K.; Danaie, M.; Tennyson, E. M.; Macpherson, S.; Abfalterer, A.; Anaya, M.; Chiang, Y.-H.; Crout, P.; Ruggeri, F. S.; Collins, S.; Grey, C. P.; Walsh, A.; Midgley, P. A.; Stranks, S. D. Stabilized Tilted-Octahedra Halide Perovskites Inhibit Local Formation of Performance-Limiting Phases. *Science* **2021**, *374* (6575), 1598–1605. https://doi.org/10.1126/science.abl4890.

(48) Greve, C.; Ramming, P.; Griesbach, M.; Leupold, N.; Moos, R.; Köhler, A.; Herzig, E. M.; Panzer, F.; Grüninger, H. To Stop or to Shuttle Halides? The Role of an Ionic Liquid in Thermal Halide Mixing of Hybrid Perovskites. *ACS Energy Lett.* **2023**, *8* (12), 5041–5049. https://doi.org/10.1021/acsenergylett.3c01878.

(49) Duijnstee, E. A.; Gallant, B. M.; Holzhey, P.; Kubicki, D. J.; Collavini, S.; Sturdza, B. K.; Sansom, H. C.; Smith, J.; Gutmann, M. J.; Saha, S.; Gedda, M.; Nugraha, M. I.; Kober-Czerny, M.; Xia, C.;

Wright, A. D.; Lin, Y.-H.; Ramadan, A. J.; Matzen, A.; Hung, E. Y.-H.; Seo, S.; Zhou, S.; Lim, J.; Anthopoulos, T. D.; Filip, M. R.; Johnston, M. B.; Nicholas, R. J.; Delgado, J. L.; Snaith, H. J. Understanding the Degradation of Methylenediammonium and Its Role in Phase-Stabilizing Formamidinium Lead Triiodide. *J. Am. Chem. Soc.* **2023**, *145* (18), 10275–10284. https://doi.org/10.1021/jacs.3c01531.

(50) Sarkar, D.; Hooper, R. W.; Karmakar, A.; Bhattacharya, A.; Pominov, A.; Terskikh, V. V.; Michaelis, V. K. Metal Halide Perovskite and Perovskite-like Materials through the Lens of Ultra-Wideline 35/37Cl NMR Spectroscopy. *ACS Materials Lett.* **2022**, *4* (7), 1255–1263. https://doi.org/10.1021/acsmaterialslett.2c00377.

(51) Hooper, R. W.; Lin, K.; Veinot, J. G. C.; Michaelis, V. K. 3D to 0D Cesium Lead Bromide: A 79/81Br NMR, NQR and Theoretical Investigation. *Journal of Magnetic Resonance* **2023**, *352*, 107472. https://doi.org/10.1016/j.jmr.2023.107472.

(52) Chen, H.; Maxwell, A.; Li, C.; Teale, S.; Chen, B.; Zhu, T.; Ugur, E.; Harrison, G.; Grater, L.; Wang, J.; Wang, Z.; Zeng, L.; Park, S. M.; Chen, L.; Serles, P.; Awni, R. A.; Subedi, B.; Zheng, X.; Xiao, C.; Podraza, N. J.; Filleter, T.; Liu, C.; Yang, Y.; Luther, J. M.; De Wolf, S.; Kanatzidis, M. G.; Yan, Y.; Sargent, E. H. Regulating Surface Potential Maximizes Voltage in All-Perovskite Tandems. *Nature* **2023**, *613* (7945), 676–681. https://doi.org/10.1038/s41586-022-05541-z.

(53) You, S.; Zeng, H.; Liu, Y.; Han, B.; Li, M.; Li, L.; Zheng, X.; Guo, R.; Luo, L.; Li, Z.; Zhang, C.; Liu, R.; Zhao, Y.; Zhang, S.; Peng, Q.; Wang, T.; Chen, Q.; Eickemeyer, F. T.; Carlsen, B.; Zakeeruddin, S. M.; Mai, L.; Rong, Y.; Grätzel, M.; Li, X. Radical Polymeric P-Doping and Grain Modulation for Stable, Efficient Perovskite Solar Modules. *Science* **2023**, *379* (6629), 288–294. https://doi.org/10.1126/science.add8786.

(54) Li, G.; Su, Z.; Canil, L.; Hughes, D.; Aldamasy, M. H.; Dagar, J.; Trofimov, S.; Wang, L.; Zuo, W.; Jerónimo-Rendon, J. J.; Byranvand, M. M.; Wang, C.; Zhu, R.; Zhang, Z.; Yang, F.; Nasti, G.; Naydenov, B.; Tsoi, W. C.; Li, Z.; Gao, X.; Wang, Z.; Jia, Y.; Unger, E.; Saliba, M.; Li, M.; Abate, A. Highly Efficient P-i-n Perovskite Solar Cells That Endure Temperature Variations. *Science* **2023**, *379* (6630), 399–403. https://doi.org/10.1126/science.add7331.

(55) Yuan, M.; Quan, L. N.; Comin, R.; Walters, G.; Sabatini, R.; Voznyy, O.; Hoogland, S.; Zhao, Y.; Beauregard, E. M.; Kanjanaboos, P.; Lu, Z.; Kim, D. H.; Sargent, E. H. Perovskite Energy Funnels for Efficient Light-Emitting Diodes. *Nature Nanotech* **2016**, *11* (10), 872–877. https://doi.org/10.1038/nnano.2016.110.

(56) Sidhik, S.; Wang, Y.; De Siena, M.; Asadpour, R.; Torma, A. J.; Terlier, T.; Ho, K.; Li, W.; Puthirath, A. B.; Shuai, X.; Agrawal, A.; Traore, B.; Jones, M.; Giridharagopal, R.; Ajayan, P. M.; Strzalka, J.; Ginger, D. S.; Katan, C.; Alam, M. A.; Even, J.; Kanatzidis, M. G.; Mohite, A. D. Deterministic Fabrication of 3D/2D Perovskite Bilayer Stacks for Durable and Efficient Solar Cells. *Science* **2022**, *377* (6613), 1425–1430. https://doi.org/10.1126/science.abq7652.

(57) Clark, S. J.; Segall, M. D.; Pickard, C. J.; Hasnip, P. J.; Probert, M. I. J.; Refson, K.; Payne, M. C. First Principles Methods Using CASTEP. *Zeitschrift für Kristallographie - Crystalline Materials* **2005**, *220* (5–6), 567–570. https://doi.org/10.1524/zkri.220.5.567.65075.

(58) Pickard, C. J.; Mauri, F. All-Electron Magnetic Response with Pseudopotentials: NMR Chemical Shifts. *Phys. Rev. B* **2001**, *63* (24), 245101. https://doi.org/10.1103/PhysRevB.63.245101.

(59) Bonhomme, C.; Gervais, C.; Babonneau, F.; Coelho, C.; Pourpoint, F.; Azaïs, T.; Ashbrook, S. E.; Griffin, J. M.; Yates, J. R.; Mauri, F.; Pickard, C. J. First-Principles Calculation of NMR Parameters Using the Gauge Including Projector Augmented Wave Method: A Chemist's Point of View. *Chem. Rev.* **2012**, *112* (11), 5733–5779. https://doi.org/10.1021/cr300108a.

(60) Bonhomme, C.; Gervais, C.; Coelho, C.; Pourpoint, F.; Azaïs, T.; Bonhomme-Coury, L.; Babonneau, F.; Jacob, G.; Ferrari, M.; Canet, D.; Yates, J. R.; Pickard, C. J.; Joyce, S. A.; Mauri, F.; Massiot, D. New Perspectives in the PAW/GIPAW Approach: JP-O-Si Coupling Constants, Antisymmetric Parts of Shift Tensors and NQR Predictions. *Magnetic Resonance in Chemistry* **2010**, *48* (S1), S86–S102. https://doi.org/10.1002/mrc.2635.

(61) Aquino, F.; Govind, N.; Autschbach, J. Electric Field Gradients Calculated from Two-Component Hybrid Density Functional Theory Including Spin−Orbit Coupling. *J. Chem. Theory Comput.* **2010**, *6* (9), 2669–2686. https://doi.org/10.1021/ct1002847.

(62) Widdifield, C. M.; Bryce, D. L. Solid-State ^{127} I NMR and GIPAW DFT Study of Metal Iodides and Their Hydrates: Structure, Symmetry, and Higher-Order Quadrupole-Induced Effects. *J. Phys. Chem. A* **2010**, *114* (40), 10810–10823. https://doi.org/10.1021/jp108237x.

(63) Szell, P. M. J.; Grébert, L.; Bryce, D. L. Rapid Identification of Halogen Bonds in Co-Crystalline Powders via ^{127} I Nuclear Quadrupole Resonance Spectroscopy. *Angew Chem Int Ed* **2019**, *58* (38), 13479–13485. https://doi.org/10.1002/anie.201905788.

(64) Yamaguchi, K.; Miyagi, H. Structure of Iodine under Pressure: Consistent Explanation for Mössbauer and X-Ray Experiments. *Solid State Communications* **1996**, *99* (2), 89–92. https://doi.org/10.1016/S0038-1098(96)80055-X.

(65) Perdew, J. P.; Burke, K.; Ernzerhof, M. Generalized Gradient Approximation Made Simple. *Phys. Rev. Lett.* **1996**, *77* (18), 3865–3868. https://doi.org/10.1103/PhysRevLett.77.3865.

(66) Even, J.; Pedesseau, L.; Jancu, J.-M.; Katan, C. Importance of Spin–Orbit Coupling in Hybrid Organic/Inorganic Perovskites for Photovoltaic Applications. *J. Phys. Chem. Lett.* **2013**, *4* (17), 2999–3005. https://doi.org/10.1021/jz401532q.

(67) Arcisauskaite, V.; Knecht, S.; Sauer, S. P. A.; Hemmingsen, L. Electric Field Gradients in Hg Compounds: Molecular Orbital (MO) Analysis and Comparison of 4-Component and 2-Component (ZORA) Methods. *Phys. Chem. Chem. Phys.* **2012**, *14* (46), 16070–16079. https://doi.org/10.1039/C2CP42291C.

(68) Tran, F.; Blaha, P.; Betzinger, M.; Blügel, S. Comparison between Exact and Semilocal Exchange Potentials: An All-Electron Study for Solids. *Phys. Rev. B* **2015**, *91* (16), 165121. https://doi.org/10.1103/PhysRevB.91.165121.

(69) Widdifield, C. M.; Zakeri, F. Can Simple 'Molecular' Corrections Outperform Projector Augmented-Wave Density Functional Theory in the Prediction of 35Cl Electric Field Gradient Tensor Parameters for Chlorine-Containing Crystalline Systems? *Magnetic Resonance in Chemistry* **2024**, *62* (3), 156–168. https://doi.org/10.1002/mrc.5408.

(70) Cuny, J.; Gautier, R.; Halet, J.-F. First-Principles Computation of NMR Parameters in Solid-State Chemistry. In *Handbook of Solid State Chemistry*; John Wiley & Sons, Ltd, 2017; pp 607–646. https://doi.org/10.1002/9783527691036.hsscvol5021.

(71) Balvanz, A.; Safdari, M.; Zacharias, M.; Kim, D.; Welton, C.; Oriel, E. H.; Kepenekian, M.; Katan, C.; Malliakas, C. D.; Even, J.; Klepov, V.; Manjunatha Reddy, G. N.; Schaller, R. D.; Chen, L. X.; Seshadri, R.; Kanatzidis, M. G. Structural Evolution and Photoluminescence Quenching across the FASnI3–xBrx (x = 0–3) Perovskites. *J. Am. Chem. Soc.* **2024**, *146* (23), 16128–16147. https://doi.org/10.1021/jacs.4c03669.

(72) Quarti, C.; Mosconi, E.; Ball, J. M.; D'Innocenzo, V.; Tao, C.; Pathak, S.; Snaith, H. J.; Petrozza, A.; Angelis, F. D. Structural and Optical Properties of Methylammonium Lead Iodide across the Tetragonal to Cubic Phase Transition: Implications for Perovskite Solar Cells. *Energy Environ. Sci.* **2016**, *9* (1), 155–163. https://doi.org/10.1039/C5EE02925B.

(73) Zhao, X.-G.; Dalpian, G. M.; Wang, Z.; Zunger, A. Polymorphous Nature of Cubic Halide Perovskites. *Phys. Rev. B* **2020**, *101* (15), 155137. https://doi.org/10.1103/PhysRevB.101.155137.

(74) Zacharias, M.; Volonakis, G.; Giustino, F.; Even, J. Anharmonic Electron-Phonon Coupling in Ultrasoft and Locally Disordered Perovskites. *npj Comput Mater* **2023**, *9* (1), 1–13. https://doi.org/10.1038/s41524-023-01089-2.

(75) Dirin, D. N.; Vivani, A.; Zacharias, M.; Sekh, T. V.; Cherniukh, I.; Yakunin, S.; Bertolotti, F.; Aebli, M.; Schaller, R. D.; Wieczorek, A.; Siol, S.; Cancellieri, C.; Jeurgens, L. P. H.; Masciocchi, N.; Guagliardi, A.; Pedesseau, L.; Even, J.; Kovalenko, M. V.; Bodnarchuk, M. I. Intrinsic Formamidinium Tin Iodide Nanocrystals by Suppressing the Sn(IV) Impurities. *Nano Lett.* **2023**, *23* (5), 1914–1923. https://doi.org/10.1021/acs.nanolett.2c04927.

(76) Zacharias, M.; Giustino, F. Theory of the Special Displacement Method for Electronic Structure Calculations at Finite Temperature. *Phys. Rev. Res.* **2020**, *2* (1), 013357. https://doi.org/10.1103/PhysRevResearch.2.013357.
(77) Zacharias, M.; Volonakis, G.; Giustino, F.; Even, J. Anharmonic Lattice Dynamics via the Special Displacement Method. *Phys. Rev. B* **2023**, *108* (3), 035155. https://doi.org/10.1103/PhysRevB.108.035155.
(78) Lee, H.; Poncé, S.; Bushick, K.; Hajinazar, S.; Lafuente-Bartolome, J.; Leveillee, J.; Lian, C.; Lihm, J.-M.; Macheda, F.; Mori, H.; Paudyal, H.; Sio, W. H.; Tiwari, S.; Zacharias, M.; Zhang, X.; Bonini, N.; Kioupakis, E.; Margine, E. R.; Giustino, F. Electron–Phonon Physics from First Principles Using the EPW Code. *npj Comput Mater* **2023**, *9* (1), 1–26. https://doi.org/10.1038/s41524-023-01107-3.
(79) Franssen, W. M. J.; van Es, S. G. D.; Dervişoğlu, R.; de Wijs, G. A.; Kentgens, A. P. M. Symmetry, Dynamics, and Defects in Methylammonium Lead Halide Perovskites. *J. Phys. Chem. Lett.* **2017**, *8* (1), 61–66. https://doi.org/10.1021/acs.jpclett.6b02542.
(80) Poglitsch, A.; Weber, D. Dynamic Disorder in Methylammoniumtrihalogenoplumbates (II) Observed by Millimeter-wave Spectroscopy. *J. Chem. Phys.* **1987**, *87* (11), 6373–6378. https://doi.org/10.1063/1.453467.
(81) Wasylishen, R. E.; Knop, O.; Macdonald, J. B. Cation Rotation in Methylammonium Lead Halides. *Solid State Communications* **1985**, *56* (7), 581–582. https://doi.org/10.1016/0038-1098(85)90959-7.
(82) Marronnier, A.; Roma, G.; Boyer-Richard, S.; Pedesseau, L.; Jancu, J.-M.; Bonnassieux, Y.; Katan, C.; Stoumpos, C. C.; Kanatzidis, M. G.; Even, J. Anharmonicity and Disorder in the Black Phases of Cesium Lead Iodide Used for Stable Inorganic Perovskite Solar Cells. *ACS Nano* **2018**, *12* (4), 3477–3486. https://doi.org/10.1021/acsnano.8b00267.
(83) Mosconi, E.; Amat, A.; Nazeeruddin, Md. K.; Grätzel, M.; De Angelis, F. First-Principles Modeling of Mixed Halide Organometal Perovskites for Photovoltaic Applications. *J. Phys. Chem. C* **2013**, *117* (27), 13902–13913. https://doi.org/10.1021/jp4048659.
(84) Song, T.; Feng, X.; Ju, H.; Fang, T.; Zhu, F.; Liu, W.; Huang, W. Enhancing Acid, Base and UV Light Resistance of Halide Perovskite CH3NH3PbBr3 Quantum Dots by Encapsulation with ZrO2 Sol. *Journal of Alloys and Compounds* **2020**, *816* (Complete). https://doi.org/10.1016/j.jallcom.2019.152558.
(85) López, C. A.; Abia, C.; Alvarez-Galván, M. C.; Hong, B.-K.; Martínez-Huerta, M. V.; Serrano-Sánchez, F.; Carrascoso, F.; Castellanos-Gómez, A.; Fernández-Díaz, M. T.; Alonso, J. A. Crystal Structure Features of CsPbBr3 Perovskite Prepared by Mechanochemical Synthesis. *ACS Omega* **2020**, *5* (11), 5931–5938. https://doi.org/10.1021/acsomega.9b04248.
(86) Kayalvizhi, T.; Sathya, A.; Perumal, S.; Preethi Meher, K. R. S. Structural, Optoelectronic and Electrochemical Behavior of the Mechanochemically Synthesized CsPb1-xNaxBr3 (X=0 to 0.15). *Journal of Solid State Chemistry* **2023**, *323*, 123997. https://doi.org/10.1016/j.jssc.2023.123997.
(87) Katan, C.; Mercier, N.; Even, J. Quantum and Dielectric Confinement Effects in Lower-Dimensional Hybrid Perovskite Semiconductors. *Chem. Rev.* **2019**, *119* (5), 3140–3192. https://doi.org/10.1021/acs.chemrev.8b00417.
(88) Glazer, A. M. The Classification of Tilted Octahedra in Perovskites. *Acta Crystallographica Section B* **1972**, *28* (11), 3384–3392. https://doi.org/10.1107/S0567740872007976.
(89) Pedesseau, L.; Sapori, D.; Traore, B.; Robles, R.; Fang, H.-H.; Loi, M. A.; Tsai, H.; Nie, W.; Blancon, J.-C.; Neukirch, A.; Tretiak, S.; Mohite, A. D.; Katan, C.; Even, J.; Kepenekian, M. Advances and Promises of Layered Halide Hybrid Perovskite Semiconductors. *ACS Nano* **2016**, *10* (11), 9776–9786. https://doi.org/10.1021/acsnano.6b05944.
(90) Quarti, C.; Marchal, N.; Beljonne, D. Tuning the Optoelectronic Properties of Two-Dimensional Hybrid Perovskite Semiconductors with Alkyl Chain Spacers. *J. Phys. Chem. Lett.* **2018**, *9* (12), 3416–3424. https://doi.org/10.1021/acs.jpclett.8b01309.

(91) Dyksik, M.; Duim, H.; Zhu, X.; Yang, Z.; Gen, M.; Kohama, Y.; Adjokatse, S.; Maude, D. K.; Loi, M. A.; Egger, D. A.; Baranowski, M.; Plochocka, P. Broad Tunability of Carrier Effective Masses in Two-Dimensional Halide Perovskites. *ACS Energy Lett.* **2020**, *5* (11), 3609–3616. https://doi.org/10.1021/acsenergylett.0c01758.

(92) Billing, D. G.; Lemmerer, A. Synthesis, Characterization and Phase Transitions in the Inorganic–Organic Layered Perovskite-Type Hybrids [(CnH2n+1NH3)2PbI4], n = 4, 5 and 6. *Acta Cryst B* **2007**, *63* (5), 735–747. https://doi.org/10.1107/S0108768107031758.

(93) Dahlman, C. J.; Kennard, R. M.; Paluch, P.; Venkatesan, N. R.; Chabinyc, M. L.; Manjunatha Reddy, G. N. Dynamic Motion of Organic Spacer Cations in Ruddlesden–Popper Lead Iodide Perovskites Probed by Solid-State NMR Spectroscopy. *Chem. Mater.* **2021**, *33* (2), 642–656. https://doi.org/10.1021/acs.chemmater.0c03958.

(94) Lin, C.-C.; Huang, S.-J.; Wu, P.-H.; Chen, T.-P.; Huang, C.-Y.; Wang, Y.-C.; Chen, P.-T.; Radeva, D.; Petrov, O.; Gelev, V. M.; Sankar, R.; Chen, C.-C.; Chen, C.-W.; Yu, T.-Y. Direct Investigation of the Reorientational Dynamics of A-Site Cations in 2D Organic-Inorganic Hybrid Perovskite by Solid-State NMR. *Nat Commun* **2022**, *13* (1), 1513. https://doi.org/10.1038/s41467-022-29207-6.

(95) Mao, L.; Wu, Y.; Stoumpos, C. C.; Traore, B.; Katan, C.; Even, J.; Wasielewski, M. R.; Kanatzidis, M. G. Tunable White-Light Emission in Single-Cation-Templated Three-Layered 2D Perovskites (CH3CH2NH3)4Pb3Br10–xClx. *J. Am. Chem. Soc.* **2017**, *139* (34), 11956–11963. https://doi.org/10.1021/jacs.7b06143.

(96) Trots, D. M.; Myagkota, S. V. High-Temperature Structural Evolution of Caesium and Rubidium Triiodoplumbates. *Journal of Physics and Chemistry of Solids* **2008**, *69* (10), 2520–2526. https://doi.org/10.1016/j.jpcs.2008.05.007.

(97) Taylor, R. E.; Beckmann, P. A.; Bai, S.; Dybowski, C. ^{127} I and ^{207} Pb Solid-State NMR Spectroscopy and Nuclear Spin Relaxation in PbI_2 : A Preliminary Study. *J. Phys. Chem. C* **2014**, *118* (17), 9143–9153. https://doi.org/10.1021/jp5023423.

(98) Deng, Z.; Kieslich, G.; Bristowe, P. D.; Cheetham, A. K.; Sun, S. Octahedral Connectivity and Its Role in Determining the Phase Stabilities and Electronic Structures of Low-Dimensional, Perovskite-Related Iodoplumbates. *APL Materials* **2018**, *6* (11), 114202. https://doi.org/10.1063/1.5046404.

(99) Pałosz, B.; Gierlotka, S.; Wiktorowska, B.; Dziąg, D. Structures of Four New Polytypes of Lead Iodide. *Acta Cryst C* **1985**, *41* (10), 1407–1409. https://doi.org/10.1107/S010827018500796X.

(100) Mitrofanov, A.; Berencén, Y.; Sadrollahi, E.; Boldt, R.; Bodesheim, D.; Weiske, H.; Paulus, F.; Geck, J.; Cuniberti, G.; Kuc, A.; Voit, B. Molecular Engineering of Naphthalene Spacers in Low-Dimensional Perovskites. *J. Mater. Chem. C* **2023**, *11* (15), 5024–5031. https://doi.org/10.1039/D3TC00132F.

(101) Fateev, S. A.; Petrov, A. A.; Khrustalev, V. N.; Dorovatovskii, P. V.; Zubavichus, Y. V.; Goodilin, E. A.; Tarasov, A. B. Solution Processing of Methylammonium Lead Iodide Perovskite from γ-Butyrolactone: Crystallization Mediated by Solvation Equilibrium. *Chem. Mater.* **2018**, *30* (15), 5237–5244. https://doi.org/10.1021/acs.chemmater.8b01906.

(102) Kamminga, M. E.; de Wijs, G. A.; Havenith, R. W. A.; Blake, G. R.; Palstra, T. T. M. The Role of Connectivity on Electronic Properties of Lead Iodide Perovskite-Derived Compounds. *Inorg. Chem.* **2017**, *56* (14), 8408–8414. https://doi.org/10.1021/acs.inorgchem.7b01096.

(103) Stoumpos, C. C.; Malliakas, C. D.; Kanatzidis, M. G. Semiconducting Tin and Lead Iodide Perovskites with Organic Cations: Phase Transitions, High Mobilities, and Near-Infrared Photoluminescent Properties. *Inorg. Chem.* **2013**, *52* (15), 9019–9038. https://doi.org/10.1021/ic401215x.

(104) Qi, Z.; Gao, H.; Yang, X.; Chen, Y.; Zhang, F.-Q.; Qu, M.; Li, S.-L.; Zhang, X.-M. A One-Dimensional Broadband Emissive Hybrid Lead Iodide with Face-Sharing PbI6 Octahedral Chains. *Inorg. Chem.* **2021**, *60* (20), 15136–15140. https://doi.org/10.1021/acs.inorgchem.1c02732.

(105) Marchal, N.; Van Gompel, W.; Gélvez-Rueda, M. C.; Vandewal, K.; Van Hecke, K.; Boyen, H.-G.; Conings, B.; Herckens, R.; Maheshwari, S.; Lutsen, L.; Quarti, C.; Grozema, F. C.; Vanderzande, D.; Beljonne, D. Lead-Halide Perovskites Meet Donor–Acceptor Charge-Transfer Complexes. *Chem. Mater.* **2019**, *31* (17), 6880–6888. https://doi.org/10.1021/acs.chemmater.9b01289.

(106) Liu, G.; Liu, J.; Sun, Z.; Zhang, Z.; Chang, L.; Wang, J.; Tao, X.; Zhang, Q. Thermally Induced Reversible Double Phase Transitions in an Organic–Inorganic Hybrid Iodoplumbate C4H12NPbI3 with Symmetry Breaking. *Inorg. Chem.* **2016**, *55* (16), 8025–8030. https://doi.org/10.1021/acs.inorgchem.6b01143.

(107) Gao, H.; Yuan, G.-J.; Lu, Y.-N.; Zhao, S.-P.; Ren, X.-M. Inorganic–Organic Hybrid Compound with Face-Sharing Iodoplumbate Chains Showing Novel Dielectric Relaxation. *Inorganic Chemistry Communications* **2013**, *32*, 18–21. https://doi.org/10.1016/j.inoche.2013.03.017.

https://doi.org/10.1021/jacs.4c09877

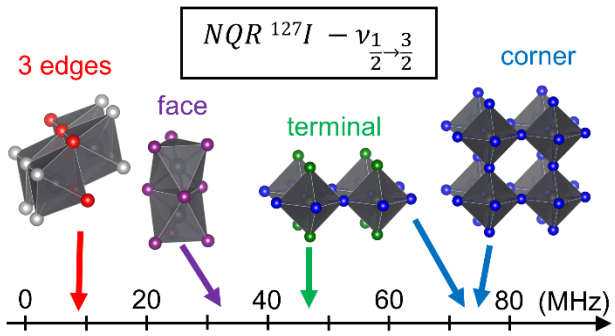

Table of Content

Characteristic Nuclear Quadrupolar Resonance (NQR) frequencies for the ^{127}I isotope in different archetypal arrangements of the lead-iodine PbI_6 octahedra with terminal or edge-, face-, corner-sharing nuclei, both in 2D and 3D.

https://doi.org/10.1021/jacs.4c09877

NQR structural characterization of halide perovskites and perovskitoids: a roadmap from electronic structure calculations for lead-iodide based compounds

SUPPORTING INFORMATION

Claudio Quarti,[a]* Régis Gautier,[b] Marios Zacharias,[c] Axel Gansmuller,[d] Claudine Katan [b]*

[a] Laboratory for Chemistry of Novel Materials, Materials Research Institute, University of Mons-UMONS, Place du Parc 20, Mons B-7000, Belgium

[b] Univ Rennes, CNRS, Ecole Nationale Supérieure de Chimie de Rennes, ISCR - UMR6226, Rennes, France

[c] Univ Rennes, CNRS, INSA Rennes, Institut FOTON - UMR6082, Rennes, France

[d] Université de Lorraine, CNRS, CRM2 UMR 7036, F-54000 Nancy, France

* corresponding authors: Claudio.QUARTI@umons.ac.be, claudine.katan@univ-rennes.fr

https://doi.org/10.1021/jacs.4c09877

Outline

Section 1. *Detailed mathematical treatment of the NQR interaction and NQR Hamiltonian for spin 3/2 and 5/2*

Section 2. *Computational details for the DFT simulations and results of the convergence tests*

Section 3. *Generation of locally disordered (polymorphous) structures*

Section 4. *Procedure for averaging the NQR properties of a compound from an ensemble of representative structural models*

Section 5. *NQR frequencies computed for the orthorhombic (γ-), tetragonal (β-) and (pseudo-)cubic (α-)phase of $CsPbI_3$ perovskite*

Section 6*. NQR frequencies computed for the γ-phase of $CsPbBr_3$ perovskite*

Section 7*. NQR frequencies of BA_2PbI_4 with explicit organic spacer and Cs-substitution*

https://doi.org/10.1021/jacs.4c09877

Section 1. *Detailed mathematical treatment of the NQR interaction and NQR Hamiltonian for spin 3/2 and 5/2*

We set here the basis of the NQR spectroscopy of nuclei with nuclear spin *I*=3/2 (for $^{35/37}$Cl and $^{79/81}$Br) and *I*=5/2 (for ^{127}I),[1] so to elucidate the information that this technique accesses. While isotopes with nuclear spin *I*=1/2 present a spherical electric charge distribution around their nucleus, those with larger nuclear spin are characterized by an oblate or prolate distribution, which gives rise to non-null nuclear electric quadrupole moment, eQ (e and Q being the elementary charge and the quadrupole moment, respectively). Besides, all nuclei in a molecule or a crystal are subject to a chemical environment, which is described by the Electric Field Gradient (EFG), defined as:

$$V_{ij} = \frac{\partial^2 V}{\partial r_i \partial r_j} \qquad \text{Eq. 1}$$

with V being the electrostatic potential experienced by the nucleus and r_i=$\{x, y, z\}$ the conventional cartesian coordinates. The EFG is a real, symmetric 3x3 tensor and, following the Laplacian equation, is traceless. It may be then conveniently described in the frame of its principal axes, using only two parameters: V_{zz} and $\eta_Q = \frac{V_{xx}-V_{yy}}{V_{zz}}$, where V_{xx}, V_{yy}, V_{zz} are the eigenvalues of the EFG tensor (with convention that $|V_{zz}| \geq |V_{yy}| \geq |V_{xx}|$). It is worth to mention that the asymmetry parameter η_Q vanishes for axially symmetric chemical environments.

NQR spectroscopy probes the interaction between the quadrupolar moment of the nucleus with the EFG, this last carrying the information about the chemical environment where an nucleus sits. The NQR Hamiltonian (H_Q) writes:[1,2]

$$H_Q = \frac{C_Q}{4I(2I-1)} \qquad \text{Eq. 2}$$

with $C_Q = eQ \cdot V_{zz}$ being the quadrupolar coupling constant; I is the nuclear spin expectation value and $\hat{I}_z, \hat{I}, \hat{I}_+, \hat{I}_-$ are the usual spin operators. All the NQR response of a nucleus is hence contained in the C_Q and η_Q parameter.

For isotopes of spin *I*=3/2 ($^{35/37}$Cl, $^{79/81}$Br), the expression of the Hamiltonian in Eq.2 in the $|I, m_I\rangle$=$\left|\frac{3}{2}, \frac{3}{2}\right\rangle$, $\left|\frac{3}{2}, \frac{1}{2}\right\rangle$, $\left|\frac{3}{2}, -\frac{1}{2}\right\rangle$, $\left|\frac{3}{2}, -\frac{3}{2}\right\rangle$ basis reads:

$$H_Q = \frac{C_q}{12}\begin{bmatrix} 3 & 0 & \eta\sqrt{3} & 0 \\ 0 & -3 & 0 & \eta\sqrt{3} \\ \eta\sqrt{3} & 0 & -3 & 0 \\ 0 & \eta\sqrt{3} & 0 & 3 \end{bmatrix} \qquad \text{Eq. 3}$$

The diagonalization of the NQR Hamiltonian in Eq. 3 leads to two sets of degenerate states. There, the NQR response of these nuclei consists in two degenerate NQR transitions with frequencies:

$$\nu_{\frac{1}{2}\leftrightarrow\frac{3}{2}} = \frac{C_Q}{2h}\sqrt{1+\frac{\eta_Q^2}{3}} \qquad \text{Eq. 4}$$

where the subscript indicates the quantum number m_I associated with the states involved in the transition. For the sake of clarity, labelling the NQR transitions with reference to the involved m_I spin quantum number is incorrect, rigorously speaking. This, because the eigenstates of the NQR Hamiltonian are pure states of the m_I operator only when the asymmetry parameter η_Q is zero. Nevertheless, in the manuscript we will always refer to the transitions as if they involve pure states of the m_I operator, for simplicity. Notice also that, for *I*=3/2, the transition may either go from

$m_I = \frac{1}{2} \rightarrow \frac{3}{2} / \frac{-3}{2} \rightarrow -\frac{1}{2}$ (Δm_I=+1) or in the opposite sense (Δm_I=-1). The direction of the transition is dictated by the sign of C_Q but this quantity is not accessible, experimentally. Though DFT is able to estimate the sign of the coupling, we will disregard about it throughout this work and will limit to report its absolute value (except when explicitly stated). Consistently, we will use the two headed arrow sign "↔" and absolute valued m_I quantum numbers. Graphical solutions of the Hamiltonian in Eq. 3 is reported in Figure S1. It is important to stress that the NQR problem of *I*=3/2 nuclei is incomplete, as the degeneracy of the two transitions leads to only one measurable NQR frequency, in presence of the two unknown quantities (C_Q and η_Q).

With the only stable isotope for Iodine (^{127}I) characterized by nuclear spin *I*=5/2, the NQR Hamiltonian in Eq. 2 expressed in the $\left|\frac{5}{2},\frac{5}{2}\right\rangle$, $\left|\frac{5}{2},\frac{3}{2}\right\rangle$, $\left|\frac{5}{2},\frac{1}{2}\right\rangle$, $\left|\frac{5}{2},-\frac{1}{2}\right\rangle$, $\left|\frac{5}{2},-\frac{3}{2}\right\rangle$ and $\left|\frac{5}{2},-\frac{5}{2}\right\rangle$ basis writes:

$$H_Q = C_q \begin{pmatrix} 1/4 & 0 & \eta/2\sqrt{40} & 0 & 0 & 0 \\ 0 & -1/20 & 0 & 3\eta/10\sqrt{8} & 0 & 0 \\ \eta/2\sqrt{40} & 0 & -1/5 & 0 & 3\eta/10\sqrt{8} & 0 \\ 0 & 3\eta/10\sqrt{8} & 0 & -1/5 & 0 & \eta/2\sqrt{40} \\ 0 & 0 & 3\eta/10\sqrt{8} & 0 & -1/20 & 0 \\ 0 & 0 & 0 & \eta/2\sqrt{40} & 0 & 1/4 \end{pmatrix} \quad \text{Eq. 5}$$

Diagonalization of the NQR Hamiltonian in Eq. 5 leads to three sets of doubly degenerate states and therefore to two transitions satisfying the condition Δm_I=±1, corresponding to $m_I = \frac{1}{2} \leftrightarrow \frac{3}{2}$ and $m_I = \frac{3}{2} \leftrightarrow \frac{5}{2}$ (again, we disregard about the sign of the coupling). Therefore, in contrast to the *I*=3/2 case, the NQR problem for nuclear spin *I*=5/2 is fully solvable, as it provides enough conditions to retrieve both the quadrupolar coupling C_Q and the asymmetry parameter η_Q. Closed form solutions of the Eq. 5 can be found in Ref.[3] but numerical solutions are illustrated in Figure S1. We conclude noticing a very peculiar property of the NQR Hamiltonian in Eq. 5, namely, for nuclei experiencing a chemical environment with axial symmetry (η_Q=0), it holds the condition:

$$\nu_{\frac{3}{2}\leftrightarrow\frac{5}{2}} = 2\nu_{\frac{1}{2}\leftrightarrow\frac{3}{2}} \quad \text{Eq. 6}$$

The following values of -0.0817 Barns, 0.2615 Barn and -0.6960 Barn were considered for the nuclear quadrupole moments of ^{35}Cl, ^{81}Br and ^{127}I, respectively.

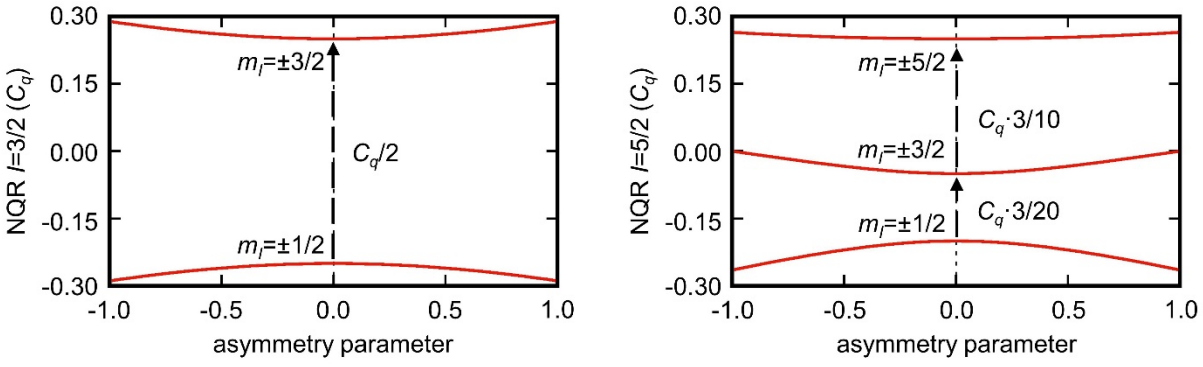

Figure S1. Solution of the NQR Hamiltonian for nuclear spin *I*=3/2 (left panel) and *I*=5/2 (right panel). Red curves are associated with the states with the indicated m_I quantum number. Energies are expressed in units of the quadrupolar coupling C_Q (assumed >0).

https://doi.org/10.1021/jacs.4c09877

Section 2. *Computational details for the DFT simulations and results of the convergence tests*

The EFG tensor components are computed with periodic DFT simulations, within the plane-wave/pseudopotential formalism, as implemented in the CASTEP suite code.[4–7] It is worth mentioning that, though relatively unexploited for the case of halide perovskites, except for Ref.[8], the DFT simulation of the NQR properties of ^{127}I has been already exploited in the past.[9–11] For instance, a pioneering study devoted to EFG of solid iodine under pressure demonstrated that DFT calculations compare very well with experimental values determined by Mössbauer spectroscopy without taking into account spin-orbit interaction.[12] All calculations reported in the main manuscript are based on the PBE functional to describe the exchange-correlation potential,[13] with relativistic effects included at the scalar relativistic level (i.e. spin-orbit-coupling (SOC) is neglected). Before performing systematic investigation of HP and perovskitoid compounds, we tested the sensitivity of the EFG estimate C_Q and η via DFT with respect to the two main computational parameters involved in these calculations. These correspond to the kinetic energy cutoff for the planewave expansion of single particle states and to the density sampling of the corresponding Bloch waves, in the reciprocal space. We performed tests on the cubic model of $CsPbX_3$ (X=Cl, Br, I) and orthorhombic model of $CsPbI_3$ (Figure S2), as available from XRD measurements reported by Baikie,[14] as well as on simplified model for 2D Cs_2PbI_4 perovskite (Figure S3).[15] Our tests show that the use of a relatively modest 400 eV planewave cutoff is sufficient to obtain practically converged results, with respect to the planewave expansion. In contrast, the estimate of C_Q is sensitive to the sampling of the reciprocal space and requires a dense *k*-point mesh of 0.02 Å^{-1}, for the considered test compounds. For instance, this set-up reduces the uncertainty related to this two computational parameters to less than 1 MHz, for the quadrupolar coupling parameter of the ^{127}I nucleus.

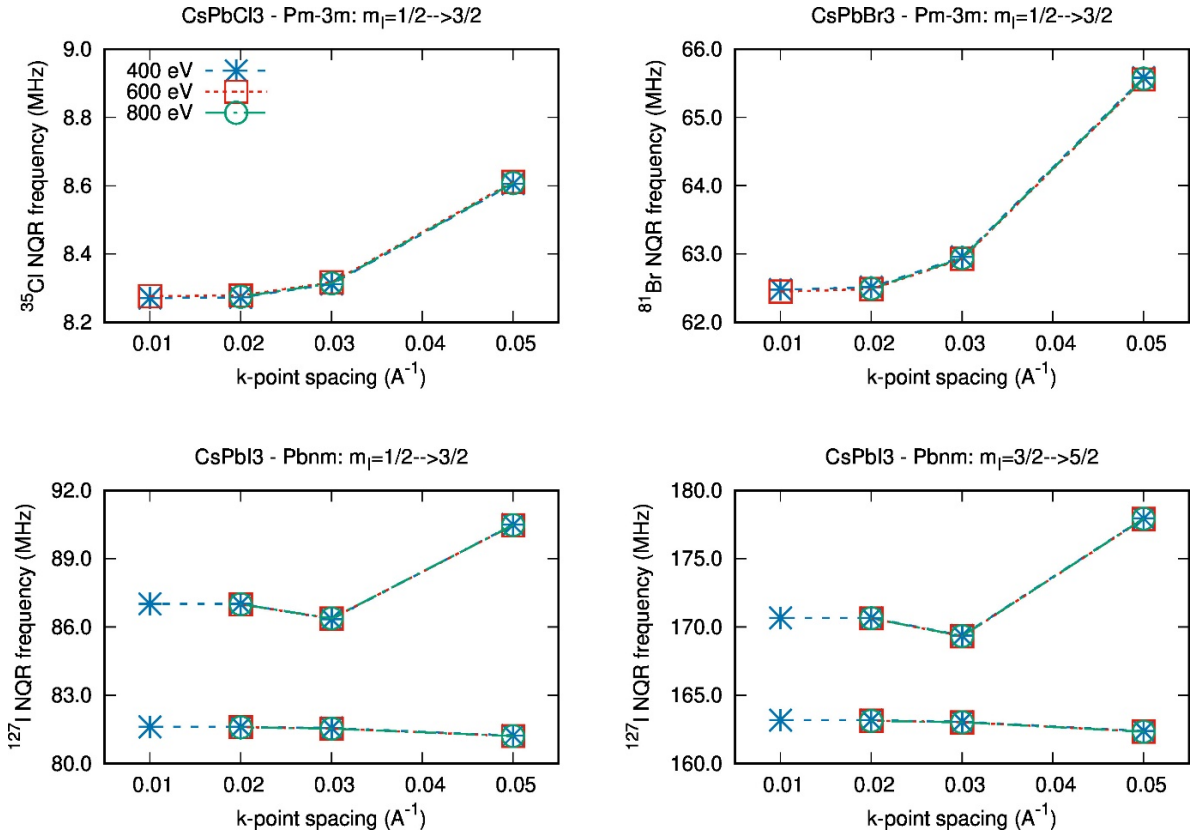

Figure S2. Dependence of the NQR resonances of cubic (*Pm-3m*) $CsPbX_3$ (X=Cl, Br) and orthorhombic (*Pbnm*) $CsPbI_3$ halide perovskites, as function of the kinetic energy cutoffs for the planewave expansion (400, 600 and 800 eV) and sampling of the reciprocal space (0.05, 0.03, 0.02 and 0.01 Å^{-1}).

https://doi.org/10.1021/jacs.4c09877

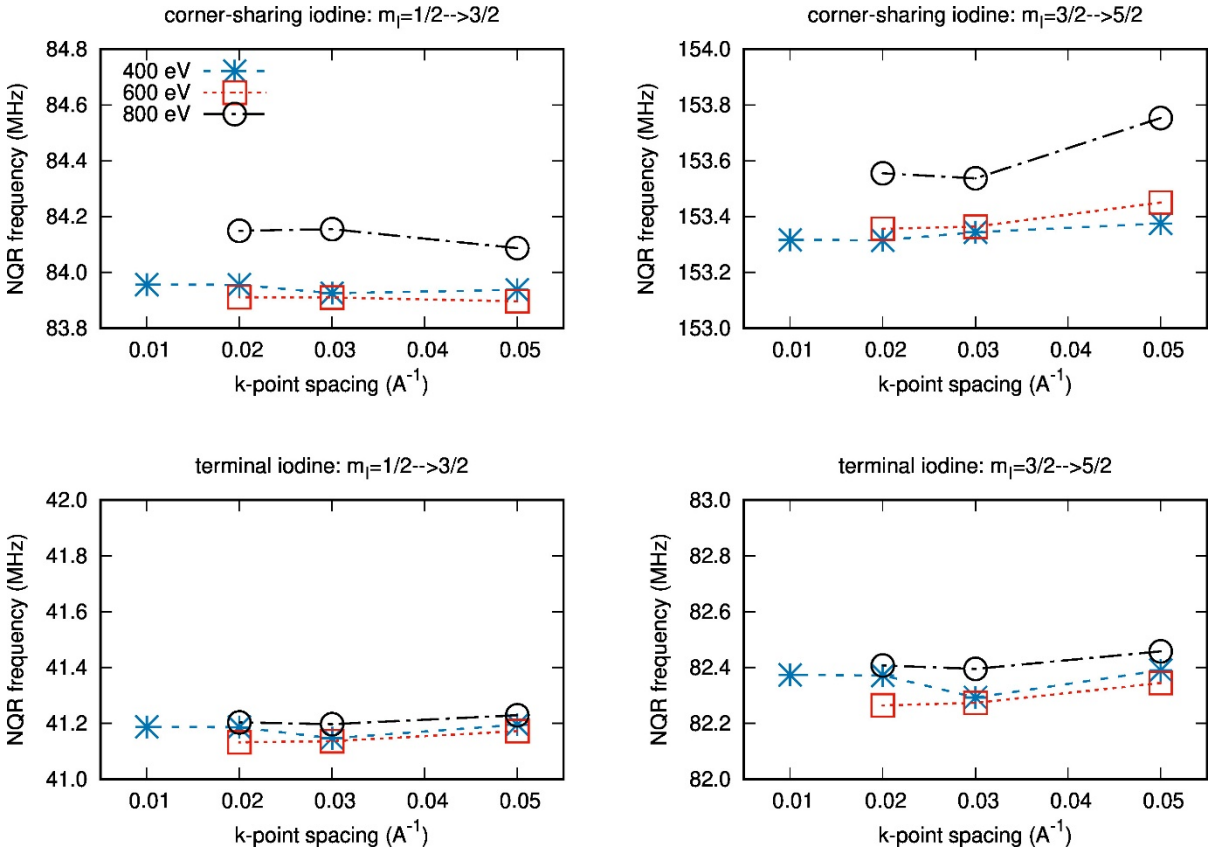

Figure S3. Dependence of the NQR resonances of 2D Cs_2PbI_4 perovskite with space group *P4mmm*, as function of the computational set-up employed for structural optimization. The position of the terminal iodines (those bound to only one lead) and Cs in the plane stacking direction is relaxed at zero K using three different kinetic energy cutoffs for the planewave expansion (400, 600 and 800 eV) and the reciprocal space sampling (0.05, 0.03, 0.02 and 0.01 $Å^{-1}$). The EFG tensor is then evaluated at fixed 400 eV, 0.02 $Å^{-1}$, so to disentangle the role of the detailed atomistic structure.

We further investigated the role of pseudopotential and of relativistic effects, in particular, SOC, beyond the scalar level. This latter is known in fact to severely impact the electronic properties of lead- and tin-based halide perovskites, in general.[16,17] With specific reference to NMR and NQR properties, in particular, a previous theoretical study by van Lenthe and Baerends performed on a set of closed shell molecules showed that the computed EFG of halogen nuclei are in most cases more influenced by scalar relativistic effect than the spin-orbit effect.[18] More recently, Sergentu *et al.* studied the $^{35/37}Cl$ NMR spectra and the ^{35}Cl and ^{79}Br NQR spectra of $Cs_2UO_2X_4$ (X= Cl, Br).[19] Their computational study showed that spin-orbit effects in the calculations are noticeable, more so for Br than for Cl. To dig more into this point, we performed additional test calculations using augmented plane wave plus local orbitals, using the WIEN2k full potential all electron program.[20] The exchange and correlation potential was computed using the GGA in the PBE parameterization. Sphere sizes were determined automatically. The calculations were converged towards the $R_{min}K_{max}$ value that controls the basis size and accuracy, and the number of k-points used for the Brillouin zone integration. The spin-orbit coupling was included in the calculations based on the second variational approach.[21]

Benchmarks performed on the cubic phase of $CsPbI_3$ highlight that the inclusion of an all-electron treatment in place of pseudopotentials, followed by the incorporation of SOC lead to the progressive increase of the C_Q parameter from 585.4 MHz to 629.0 MHz (all electron) then to 672.0 MHz (all electron+SOC). On the other hand, experimental reports for the high temperature cubic phase of $MAPbI_3$ and $FAPbI_3$ provide estimates of C_Q ranging between 549.10 MHz and 581.96 MHz.[22] Hence the coarser pseudopotential/no-SOC treatment obtained considering monomorphous structural models provides better agreement with experiment. We speculate that such agreement from the formally less accurate approach is likely due to error cancelation between lack of all electron treatment and relativistic spin-orbit coupling, inaccurate treatment of electronic correlation with the employed PBE exchange-correlation functional.[23–25] It is also worth mentioning that these differences may be partly due to structural and motional effects, as the above NQR parameters refers to frozen models obtained from experimental XRD measurements.

Section 3. *Generation of locally disordered (polymorphous) structures*

The polymorphous structures for cubic hybrid halide perovskites as well as for orthorhombic, tetragonal, and cubic $CsPbI_3$ were generated using the anharmonic special displacement method (ASDM),[26,27] as described in Ref. [28] and implemented in the EPW package,[29] of the Quantum Espresso code.[30] We first compute the dynamically unstable harmonic phonons of the high-symmetry unit cells using density functional perturbation theory,[31] and an initial random orientation of the MA or FA molecules. We build 2×2×2 supercells, choosing again a random orientation for each of the 8 molecules, and displace all nuclei along the soft modes computed for each structure. Then, we perform a geometry optimization and allow the atoms to relax with the lattice parameters constant at their experimental values. This procedure allows to accommodate local disorder in supercells manifested as octahedral tilting, off-center displacements of the metal atoms, and a random distribution of Cs, MA or FA cations. Compared to the monomorphous structures, i.e. the high-symmetry unit cells, the polymorphous structures yield significant energy lowerings of the order of 100 meV per unit cell, similar to the calculations reported in Ref. [28]. For all calculations, we used a plane wave energy cutoff of 60 Ry, the Perdew–Burke–Ernzerhof exchange–correlation functional for solids (PBEsol),[32] and optimized norm-conserving Vanderbilt pseudopotentials.[33,34] We sampled the Brillouin zone for cubic, tetragonal, and orthorhombic structures using 3×3×3, 2×2×3, 2×2×3 zone-centered **k**-grids.

Section 4. *Procedure for averaging the NQR properties of a compound from an ensemble of representative structural models*

In order to compare to the experimental observable measured in an NQR experiment, we need to average motion faster than the anisotropy of the quadrupolar interaction between the quadrupole moment and the electric field gradient at the site of the nucleus of interest.[35] To do so, we need an ensemble of structural models representative of the structural fluctuations at a given temperature. Given the polymorphous nature of metal halide perovskites, we resort here to the so called anharmonic *special displacement method* (ASDM), considering a set 10 structural models in a 2x2x2 supercell.[26,27] The same procedure could be applied considering structures obtained from conformational sampling or from molecular dynamics simulations at finite temperature, as proposed in Ref. [36], but in the NPT ensemble to capture anharmonic effects.[37]

The averaging procedure needs three steps:

1) Based on symmetry arguments, identify atomic sites having the same Wyckoff position and the same orientation of the principles axis frame (PAF) with respect to the cartesian coordinate system. For a given site, average linearly each matrix element of the EFG tensor expressed in the fixed cartesian frame.

2) Diagonalize each of the EFG tensors computed in step 1 so as to transform to the PAF. If the transformation matrix from the cartesian frame ***e*** to the PAF system ***e'*** reads ***Q*** (***e'=Qe***), ***V'=QVQ***^{T}.

3) Perform a linear average over the tensors obtained in step 2. The final tensor should respect the site symmetry.

For highly symmetric systems, the quality of the set of structural model can be verified by abruptly averaging the data. In the case of a cubic system, each tensor component averaged over all atomic sites with the same Wyckoff position should be almost vanishing. This leads to the condition $V_{xx}=V_{yy}$ (or equivalently $\eta=0$), as shown in Figure S4.

The averaging process described at the points 1-3 is crucial to retrieve the axial symmetry ($\eta=0$ or equivalently $V_{xx}=V_{yy}$) of the halides in the α-phase of 3D halide perovskites, as also found experimentally. The crude average of C_Q and η parameters (or equivalently of V_{xx}, V_{yy} and V_{zz}) leads to an incorrect averaging, as shows in Figure S4 (empty symbols), ultimately leading to a chemical environment that does not present the axial symmetry.

Using 10 structures obtained with random orientations of the organic cations in a fixed cubic inorganic frame leads to rather poor agreement with experiment (squares, Figure S4). Notice in particular that these models do not retrieve the correct axial symmetry for the halides, even when adopting the correct averaging procedure (full symbols), highlighting that these models fail in accurately simulating the chemical environment experienced by these nuclei. The condition $\eta\_Q\neq0$ is related to the fact that the number of configurations are by far too limited.

https://doi.org/10.1021/jacs.4c09877

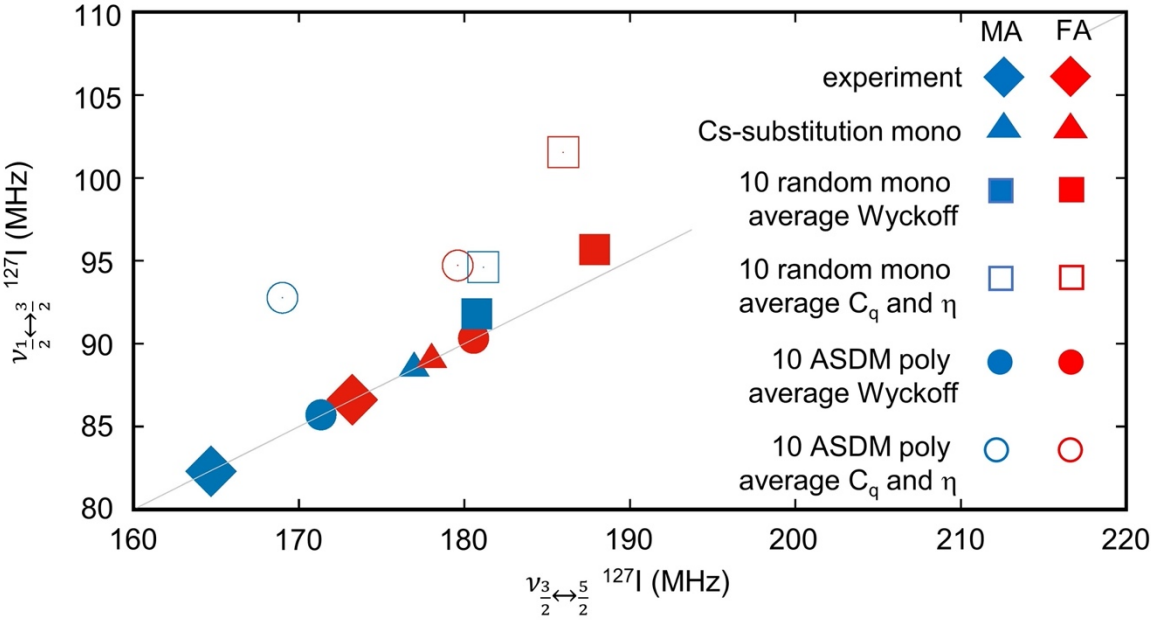

Figure S4. 2D scattering plot of the $\nu_{1/2\rightarrow 3/2}$ against $\nu_{3/2\rightarrow 5/2}$ transition frequency comparing the theoretical characteristic frequencies for $MAPbI_3$ and $FAPbI_3$, against the experiment. The theoretical estimates are obtained using the high symmetry structures with FA/MA substituted by Cs (Cs-substitution mono) or randomly oriented (10 random mono), explicit organic MA/FA cation models obtained from the anharmonic special displacement methods (ASDM poly), along with statistical average as described (average Wyckoff) or abrupt averaging of the C_Q and h parameters (average C_Q and η).

Accounting explicitly for both the dynamic disorder of the organic moiety and inorganic frame based on polymorphous structures (10 ASDM poly, Figure S4) provides better agreement with experiments as compared to the Cs-substitution strategy (triangles). Notice in particular that the experimental 4.3/8.6 MHz upshift for the $m_I = \frac{1}{2} \leftrightarrow \frac{3}{2} / m_I = \frac{3}{2} \leftrightarrow \frac{5}{2}$ transition, when going from $MAPbI_3$ to $FAPbI_3$, is reproduced to a much better extent (4.6/9.2 MHz) than with Cs-substitution (0.6/1.2 MHz).

Meanwhile, in spite of its simplicity, the Cs-substitution strategy still does provide results in similar agreement with the explicit inclusion of the organic spacer. The average absolute error for the four experimental transitions (two transitions for FA and MA) amounts to 6.2 MHz when considering the Cs-substitution, and reduces only to 5.3 MHz when explicitly considering the dynamic disorder.

Overall, these results clearly point out that even though Cs-substitution does not contain all the fundamental physical ingredients to describe the system of interest, it can be considered a good first proxy for the prediction of the NQR properties of halide perovskites and perovskitoids, especially at the light of its reduced computational cost.

https://doi.org/10.1021/jacs.4c09877

***Section 5**. NQR frequencies computed for the orthorhombic (γ-), tetragonal (β-) and (pseudo-)cubic (α-)phase of $CsPbI_3$ perovskite*

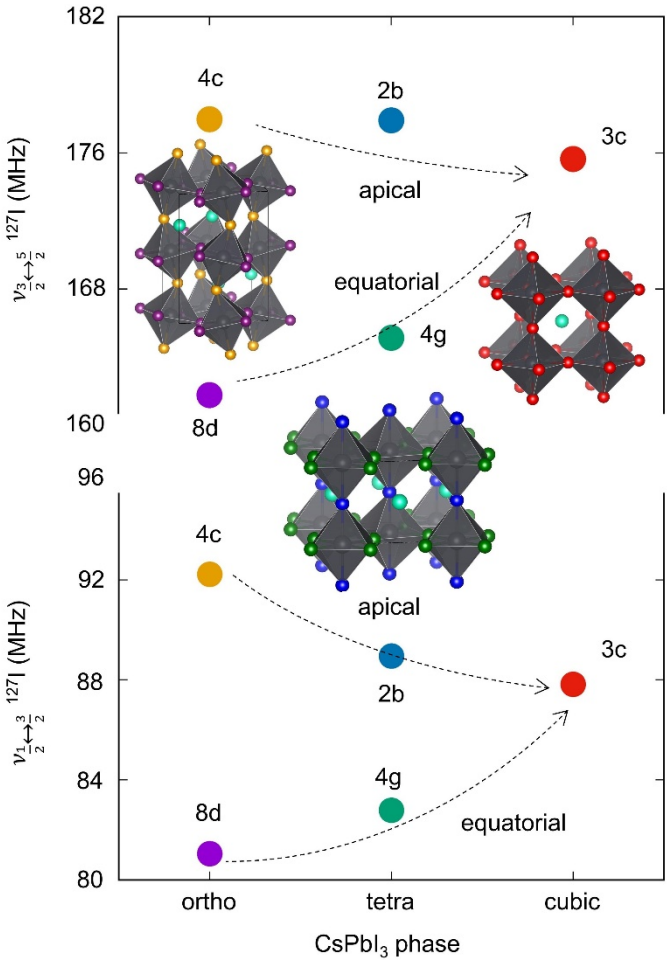

Figure S5. $\nu_{1/2\rightarrow 3/2}$ and $\nu_{3/2\rightarrow 5/2}$ ^{127}I NQR frequencies computed for the three phases of $CsPbI_3$ halide perovskite. Crystal structures come from Ref.[38]. The labels 4c/8d, 2b/4g and 3c refer to the crystal site, following the Wyckoff classifications and are further classified as apical (4c, 2b) and equatorial (8d and 4g) sites.

https://doi.org/10.1021/jacs.4c09877

Section 6. *NQR frequencies computed for the γ-phase of $CsPbBr_3$ perovskite*

We computed the NQR resonance frequencies of the γ-phase of $CsPbBr_3$, considering three high-symmetry crystalline models reported in the literature for this compound.[38–40] All models are characterized by #62 space group symmetry and all present only two inequivalent crystallographic (Wyckoff) positions, namely the 4c and 8d. Correspondingly, our DFT calculations provided only two sets of signals, that we classify accordingly to the Wyckoff positions 4c and 8d. The results are compared with the experimental data from Ref. [41]

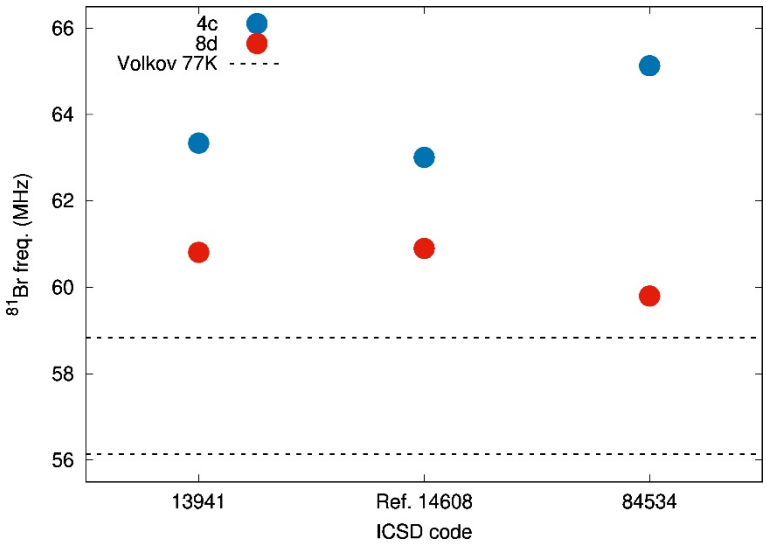

Figure S6. Theoretical NQR frequencies for the γ-phase of $CsPbBr_3$, as predicted considering the three orthorhombic structures from XRD characterization reported in the ICSD. The dashed lines refer to the two high frequency experimental signals reported in Ref.[41], recorded at 77 K.

https://doi.org/10.1021/jacs.4c09877

Section 7. *NQR frequencies of BA_2PbI_4 with explicit organic spacer and Cs-substitution*

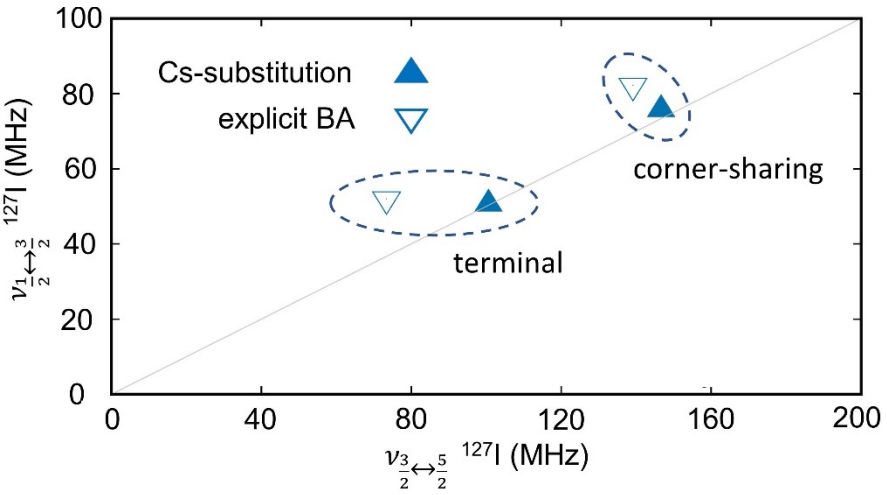

Figure S7. Comparison of the theoretical ^{127}I NQR frequencies of BA_2PbI_4 (BA=butylammonium), computed while explicitly considering the BA spacer or substituting it with Cs at the position of the nitrogen atom (Cs-substitution). The inorganic frame is taken from the XRD structure reported in Ref.[42] and the atomic positions of the BA cation have been relaxed.

References

[1] B. H. Suits, in *Handbook of Applied Solid State Spectroscopy* (Ed.: D. R. Vij), Springer US, Boston, MA, **2006**, pp. 65–96.
[2] T. P. Das, E. L. Hann, *Nuclear Quadrupole Resonance Spectroscopy*, Academic Press, NY, **1958**.
[3] G. K. Semin, *Russ. J. Phys. Chem.* **2007**, *81*, 38.
[4] S. J. Clark, M. D. Segall, C. J. Pickard, P. J. Hasnip, M. I. J. Probert, K. Refson, M. C. Payne, *Zeitschrift für Kristallographie - Crystalline Materials* **2005**, *220*, 567.
[5] C. J. Pickard, F. Mauri, *Phys. Rev. B* **2001**, *63*, 245101.
[6] C. Bonhomme, C. Gervais, F. Babonneau, C. Coelho, F. Pourpoint, T. Azaïs, S. E. Ashbrook, J. M. Griffin, J. R. Yates, F. Mauri, C. J. Pickard, *Chem. Rev.* **2012**, *112*, 5733.
[7] C. Bonhomme, C. Gervais, C. Coelho, F. Pourpoint, T. Azaïs, L. Bonhomme-Coury, F. Babonneau, G. Jacob, M. Ferrari, D. Canet, J. R. Yates, C. J. Pickard, S. A. Joyce, F. Mauri, D. Massiot, *Magnetic Resonance in Chemistry* **2010**, *48*, S86.
[8] D. Sarkar, R. W. Hooper, A. Karmakar, A. Bhattacharya, A. Pominov, V. V. Terskikh, V. K. Michaelis, *ACS Materials Lett.* **2022**, *4*, 1255.
[9] F. Aquino, N. Govind, J. Autschbach, *J. Chem. Theory Comput.* **2010**, *6*, 2669.
[10] C. M. Widdifield, D. L. Bryce, *J. Phys. Chem. A* **2010**, *114*, 10810.
[11] P. M. J. Szell, L. Grébert, D. L. Bryce, *Angew Chem Int Ed* **2019**, *58*, 13479.
[12] K. Yamaguchi, H. Miyagi, *Solid State Communications* **1996**, *99*, 89.
[13] J. P. Perdew, K. Burke, M. Ernzerhof, *Phys. Rev. Lett.* **1996**, *77*, 3865.
[14] T. Baikie, Y. Fang, J. M. Kadro, M. Schreyer, F. Wei, S. G. Mhaisalkar, M. Graetzel, T. J. White, *J. Mater. Chem. A* **2013**, *1*, 5628.
[15] C. Quarti, G. Giorgi, C. Katan, J. Even, M. Palummo, *Advanced Optical Materials* **2024**, *12*, 2202801.
[16] J. Even, L. Pedesseau, J.-M. Jancu, C. Katan, *J. Phys. Chem. Lett.* **2013**, *4*, 2999.
[17] J. Even, L. Pedesseau, C. Katan, M. Kepenekian, J.-S. Lauret, D. Sapori, E. Deleporte, *J. Phys. Chem. C* **2015**, *119*, 10161.
[18] E. van Lenthe, E. Jan Baerends, *The Journal of Chemical Physics* **2000**, *112*, 8279.
[19] D.-C. Sergentu, F. Gendron, E. D. Walter, S. Park, C. Capan, R. G. Surbella, C. Z. Soderquist, G. B. Hall, S. I. Sinkov, J. Autschbach, H. Cho, *Inorganic Chemistry* **2021**, DOI 10.1021/acs.inorgchem.1c02832.
[20] P. Blaha, K. Schwarz, F. Tran, R. Laskowski, G. K. H. Madsen, L. D. Marks, *The Journal of Chemical Physics* **2020**, *152*, 074101.
[21] J. Kuneš, P. Novák, R. Schmid, P. Blaha, K. Schwarz, *Phys. Rev. B* **2001**, *64*, 153102.
[22] K. Yamada, S. Hino, S. Hirose, Y. Yamane, I. Turkevych, T. Urano, H. Tomiyasu, H. Yamagishi, S. Aramaki, *Bulletin of the Chemical Society of Japan* **2018**, *91*, 1196.
[23] V. Arcisauskaite, S. Knecht, S. P. A. Sauer, L. Hemmingsen, *Phys. Chem. Chem. Phys.* **2012**, *14*, 16070.
[24] F. Tran, P. Blaha, M. Betzinger, S. Blügel, *Phys. Rev. B* **2015**, *91*, 165121.
[25] C. M. Widdifield, F. Zakeri, *Magnetic Resonance in Chemistry* **2024**, *62*, 156.
[26] M. Zacharias, F. Giustino, *Phys. Rev. Res.* **2020**, *2*, 013357.
[27] M. Zacharias, G. Volonakis, F. Giustino, J. Even, *Phys. Rev. B* **2023**, *108*, 035155.
[28] M. Zacharias, G. Volonakis, F. Giustino, J. Even, *npj Comput Mater* **2023**, *9*, 1.
[29] H. Lee, S. Poncé, K. Bushick, S. Hajinazar, J. Lafuente-Bartolome, J. Leveillee, C. Lian, J.-M. Lihm, F. Macheda, H. Mori, H. Paudyal, W. H. Sio, S. Tiwari, M. Zacharias, X. Zhang, N. Bonini, E. Kioupakis, E. R. Margine, F. Giustino, *npj Comput Mater* **2023**, *9*, 1.
[30] P. Giannozzi, O. Andreussi, T. Brumme, O. Bunau, M. B. Nardelli, M. Calandra, R. Car, C. Cavazzoni, D. Ceresoli, M. Cococcioni, N. Colonna, I. Carnimeo, A. D. Corso, S. de Gironcoli, P. Delugas, R. A. DiStasio, A. Ferretti, A. Floris, G. Fratesi, G. Fugallo, R. Gebauer, U. Gerstmann, F. Giustino, T. Gorni, J. Jia, M. Kawamura, H.-Y. Ko, A. Kokalj, E. Küçükbenli, M. Lazzeri, M. Marsili, N. Marzari, F. Mauri, N. L. Nguyen, H.-V. Nguyen, A. Otero-de-la-Roza, L. Paulatto, S. Poncé, D.

Rocca, R. Sabatini, B. Santra, M. Schlipf, A. P. Seitsonen, A. Smogunov, I. Timrov, T. Thonhauser, P. Umari, N. Vast, X. Wu, S. Baroni, *J. Phys.: Condens. Matter* **2017**, *29*, 465901.
[31] S. Baroni, S. de Gironcoli, A. Dal Corso, P. Giannozzi, *Rev. Mod. Phys.* **2001**, *73*, 515.
[32] J. P. Perdew, A. Ruzsinszky, G. I. Csonka, O. A. Vydrov, G. E. Scuseria, L. A. Constantin, X. Zhou, K. Burke, *Phys. Rev. Lett.* **2008**, *100*, 136406.
[33] D. R. Hamann, *Phys. Rev. B* **2013**, *88*, 085117.
[34] M. J. van Setten, M. Giantomassi, E. Bousquet, M. J. Verstraete, D. R. Hamann, X. Gonze, G.-M. Rignanese, *Computer Physics Communications* **2018**, *226*, 39.
[35] V. Diez-Gómez, P. L. de Andres, J. Sanz, *ChemSusChem* **2020**, *13*, 1027.
[36] S. Grimme, C. Bannwarth, S. Dohm, A. Hansen, J. Pisarek, P. Pracht, J. Seibert, F. Neese, *Angewandte Chemie International Edition* **2017**, *56*, 14763.
[37] M. A. Carignano, S. A. Aravindh, I. S. Roqan, J. Even, C. Katan, *J. Phys. Chem. C* **2017**, *121*, 20729.
[38] T. Song, X. Feng, H. Ju, T. Fang, F. Zhu, W. Liu, W. Huang, *Journal of Alloys and Compounds* **2020**, *816*, DOI 10.1016/j.jallcom.2019.152558.
[39] C. A. López, C. Abia, M. C. Alvarez-Galván, B.-K. Hong, M. V. Martínez-Huerta, F. Serrano-Sánchez, F. Carrascoso, A. Castellanos-Gómez, M. T. Fernández-Díaz, J. A. Alonso, *ACS Omega* **2020**, *5*, 5931.
[40] T. Kayalvizhi, A. Sathya, S. Perumal, K. R. S. Preethi Meher, *Journal of Solid State Chemistry* **2023**, *323*, 123997.
[41] A. F. Volkov, Yu. N. Venevtsev, G. K. Semin, *physica status solidi (b)* **1969**, *35*, K167.
[42] D. G. Billing, A. Lemmerer, *Acta Cryst B* **2007**, *63*, 735.